The Astronomical Journal, 136:919–945, 2008 September doi:10.1088/0004-6256/136/3/919

SPITZER SURVEY OF THE LARGE MAGELLANIC CLOUD, SURVEYING THE AGENTS OF A GALAXY'S EVOLUTION (SAGE). IV. DUST PROPERTIES IN THE INTERSTELLAR MEDIUM

Jean-Philippe Bernard[1], William T. Reach[2], Deborah Paradis[1], Margaret Meixner[3], Roberta Paladini[2], Akiko Kawamura[4], Toshikazu Onishi[4], Uma Vijh[3], Karl Gordon[5], Remy Indebetouw[6], Joseph L. Hora[7], Barbara Whitney[8], Robert Blum[9], Marilyn Meade[10], Brian Babler[10], Ed B. Churchwell[10], Charles W. Engelbracht[11], Bi-Qing For[11], Karl Misselt[11], Claus Leitherer[3], Martin Cohen[12], François Boulanger[13], Jay A. Frogel[14], Yasuo Fukui[4], Jay Gallagher[8], Varoujan Gorjian[15], Jason Harris[11], Douglas Kelly[11], William B. Latter[2], Suzanne Madden[16], Ciska Markwick-Kemper[6], Akira Mizuno[4], Norikazu Mizuno[4], Jeremy Mould[17], Antonella Nota[3], M. S. Oey[18], Knut Olsen[11], Nino Panagia[3], Pablo Perez-Gonzalez[11], Hiroshi Shibai[4], Shuji Sato[4], Linda Smith[19], Lister Staveley-Smith[20], A. G. G. M. Tielens[21], Toshiya Ueta[21], Schuyler Van Dyk[2], Kevin Volk[22], Michael Werner[15], and Dennis Zaritsky[11]

[1] CESR, Toulouse, France
[2] *Spitzer* Science Center, Caltech, MS 220-6, Pasadena, CA 91125, USA
[3] Space Telescope Science Institute, 3700 San Martin Drive, Baltimore, MD 21218, USA
[4] Department of Astrophysics, Nagoya University, Chikusa-Ku, Nagoya 464-01, Japan
[5] Steward Observatory, University of Arizona, 933 North Cherry Ave., Tucson, AZ 85721, USA
[6] Department of Astronomy, University of Virginia, P.O. Box 3818, Charlottesville, VA 22903-0818, USA
[7] Harvard-Smithsonian, CfA, 60 Garden St., MS 65, Cambridge, MA 02138-1516, USA
[8] Space Science Institute, 4750 Walnut St., Suite 205, Boulder, CO 80301, USA
[9] Cerro Tololo Interamerican Observatory, Casilla 603, la Serena, Chile
[10] Department of Astronomy, University of Wisconsin–Madison, 475 N. Charter St., Madison, WI 53706, USA
[11] Steward Observatory, University of Arizona, 933 North Cherry Ave., Tucson, AZ 85721, USA
[12] University of California, Berkeley, Radio Astronomy Lab., 601 Campbell Hall, Berkeley, CA 94720-3411, USA
[13] Institut d'Astrophsique Spatiale, Université Paris XI, Orsay, France
[14] AURA, Inc., 1200 New York Avenue, NW, Suite 350, Washington, DC, 20005, USA
[15] Jet Propulsion Laboratory, 4800 Oak Grove Blvd., MS 169-327, Pasadena, CA 91109, USA
[16] Service d'Astrophysique, CEA, Saclay, 91191 Gif-Sur-Yvette Cedex, France
[17] National Optical Astronomy Observatory, 950 N. Cherry Ave., Tucson, AZ 85726-6732, USA
[18] Department of Astronomy, University of Michigan, 830 Dennison Bldg., Ann Arbor, MI 48109, USA
[19] Department of Physics and Astronomy, University College London, Gower St., London WC1E 6BT, UK
[20] Commonwealth Science and Industrial Research Organization (CSIRO), Head Office, GPO Box 4908, Melbourne, VIC 3001 Australia
[21] NASA Ames Research Center, Mail Stop 211-3, SOFIA, Moffett Field, CA 94035, USA
[22] Gemini Observatory, Northern Operations Center, 670 N. Aohuku Place, Hilo, HI 96720, USA
Received 2007 November 8; accepted 2008 April 28; published 2008 July 21

ABSTRACT

The goal of this paper is to present the results of a preliminary analysis of the extended infrared (IR) emission by dust in the interstellar medium (ISM) of the Large Magellanic Cloud (LMC). We combine *Spitzer* Surveying the Agents of Galaxy Evolution (SAGE) and *Infrared Astronomical Satellite* (*IRAS*) data and correlate the infrared emission with gas tracers of H I, CO, and H_α. We present a global analysis of the infrared emission as well as detailed modeling of the spectral energy distribution (SED) of a few selected regions. Extended emission by dust associated with the neutral, molecular, and diffuse ionized phases of the ISM is detected at all IR bands from 3.6 μm to 160 μm. The relative abundance of the various dust species appears quite similar to that in the Milky Way (MW) in all the regions we have modeled. We construct maps of the temperature of large dust grains. The temperature map shows variations in the range 12.1–34.7 K, with a systematic gradient from the inner to outer regions, tracing the general distribution of massive stars and individual H II regions as well as showing warmer dust in the stellar bar. This map is used to derive the far-infrared (FIR) optical depth of large dust grains. We find two main departures in the LMC with respect to expectations based on the MW: (1) excess mid-infrared (MIR) emission near 70 μm, referred to as the 70 μm excess, and (2) departures from linear correlation between the FIR optical depth and the gas column density, which we refer to as FIR excess emission. The 70 μm excess increases gradually from the MW to the LMC to the Small Magellanic Cloud (SMC), suggesting evolution with decreasing metallicity. The excess is associated with the neutral and diffuse ionized gas, with the strongest excess region located in a loop structure next to 30 Dor. We show that the 70 μm excess can be explained by a modification of the size distribution of very small grains with respect to that in the MW, and a corresponding mass increase of $\simeq$13% of the total dust mass in selected regions. The most likely explanation is that the 70 μm excess is due to the production of large very small grains (VSG) through erosion of larger grains in the diffuse medium. This FIR excess could be due to intrinsic variations of the dust/gas ratio, which would then vary from 4.6 to 2.3 times lower than the MW values across the LMC, but X_{CO} values derived from the IR emission would then be about three times lower than those derived from the Virial analysis of the CO data. We also investigate the possibility that the FIR excess is associated with an additional gas component undetected in the available gas tracers. Assuming a constant dust abundance in all ISM phases, the additional gas component would have twice the known

H I mass. We show that it is plausible that the FIR excess is due to cold atomic gas that is optically thick in the 21 cm line, while the contribution by a pure H_2 phase with no CO emission remains a possible explanation.

Key words: galaxies: ISM – infrared: galaxies – infrared: ISM – ISM: abundances – ISM: clouds – Magellanic Clouds

Online-only material: color figures

1. INTRODUCTION

The Large Magellanic Cloud (LMC) is among the external galaxies nearest to our own ($\simeq$50 kpc, Keller et al. 2006; Feast 1999) after the Sagittarius and Canis Major dwarf galaxies which lie close to the Milky Way (MW) plane. It is also conveniently oriented almost face-on (viewing angle of 35°, Van der Marel & Cioni 2001), which should allow the study of the interstellar medium (ISM) emission with almost no confusion along the line of sight. The LMC is known for its low-metallicity ($Z \simeq 0.3$–$0.5\,Z_\odot$, Westerlund 1997; $Z \simeq 1/4$, Dufour 1984), similar to that prevailing in early star-forming galaxies (Pei et al. 1999). Note that taking into account the substantial revision (Asplund et al. 2004, 12+log(O/H) = 8.66+/−0.05) that brought the Sun's abundance more in line with that of the local ISM and B-stars, the LMC metallicity proposed by Dufour (1984) would be about 1/2 solar.

There are indications that dust in low-metallicity galaxies is globally different than in metal-rich galaxies. For instance, from the modeling of the ultraviolet (UV) to millimeter spectral energy distribution (SED) of a sample of low-metallicity galaxies, Galliano et al. (2003, 2005) inferred polycyclic aromatic hydrocarbon (PAH) relative abundances much lower than in the MW, but they also found that the global SED from the mid-infrared (MIR) to the far-infrared (FIR) is dominated by emission from much smaller dust grain sizes (3–4 nm) than in the MW. They argued that dust grains emitting at wavelengths as long as 100 μm were stochastically heated, in contrast to the larger dust grains dominating the diffuse emission in the MW. They also presented evidence for the presence of very cold ($T_d < 9$ K) dust to explain the observed submm/mm excess observed.

In the LMC, detailed studies of the extinction curve (e.g., Misselt et al. 1999; Clayton & Martin 1985; Gordon et al. 2003) have shown that the majority of the extinction curves measured in the LMC are significantly different than those in the MW, with a smaller UV bump and a steeper far-ultraviolet (FUV) rise, while some are similar. Conversely, the shape of the LMC extinction curve is similar to that in the MW in the visible and near-infrared (NIR) (e.g., Clayton & Martin 1985). Also, the bump size and FUV rise are anticorrelated, both in the LMC and in the MW (Massa & Savage 1984).

Although it is difficult to disentangle from selection effects, it is likely that there is a continuum of dust properties from Small Magellanic Cloud (SMC) to our own MW, as well as within the LMC. Gordon et al. (2003) argued that these changes could be linked to variations of the dust properties while going from quiescent to active regions of the LMC. These studies also measured the N_H/Av ratio along lines of sight toward the stars where the extinction curve is measured. The average value for the LMC is $N_{H\,I}/Av = 3.25 \times 10^{21}$ cm^{-2}. Compared to the average galactic value of $N_{H\,I}/Av = 1.55 \times 10^{21}$ cm^{-2} (Bohlin et al. 1978; Diplas et al. 1994). This indicates an average dust content in the LMC about 2.6 times lower than in the MW, consistent with its lower metallicity, under the naive assumption of a dust-to-gas ratio proportional to metallicity. However, large variations of this ratio seem to exist. For instance, the LMC2 super shell (corresponding to SGS19 in the nomenclature of Kim et al. 2003) next to 30 Dor has an average $N_{H\,I}/Av = 6.97 \times 10^{21}$ cm^{-2} (5.6 times lower dust abundance than the MW) according to Gordon et al. (2003). Similarly, Clayton & Martin (1985) suggested that the steep FUV rise and lower bump may be a characteristic specific to stars close to the 30 Dor region, while stars away from it seemed to be less extreme and more similar to MW extinction curves. However, this effect was of marginal significance in their data, given the estimated error bars.

Polarization of the extinction also indicates a similar behavior as in our Galaxy, in particular with a similar value of the maximum polarization parameter $p_{max}/E(B-V)$ of about 5% mag^{-1}, but also regarding the relationship between p_{max} and reddening and the relationship between the wavelength of maximum polarization λ_{max} and the ratio of total to selective extinction R (Clayton et al. 1983). This indicates that the variations observed in the UV absorption curve are probably related to changes of the dust composition, which do not affect the polarization or the shape of the visible extinction. This picture is consistent with dust models where the UV bump and FUV rise are produced by small dust particles, while visible extinction is produced by a different dust population with larger sizes (see Désert et al. 1990) where the smallest dust particles do not contribute significantly to the observed polarization.

Given the paucity of IR data with the appropriate sky coverage and angular resolution toward the LMC prior to the Surveying the Agents of Galaxy Evolution (SAGE) data, very few studies have focused on large-scale analysis of the dust emission over the LMC. Aguirre et al. (2003) obtained sub-millimeter measurements of the LMC emission from 470 μm to 1.2 mm with the top-hat balloon-borne experiment. Applying a single temperature gray body fit to their data and Diffuse Infrared Background Experiment (DIRBE) data at 100, 140, and 240 μm to the LMC SED with the 30 Dor contribution subtracted, they derived an average dust temperature of $T = 25.0 \pm 1.8$ K in the ISM and a dust emissivity power-law index of $\beta = 1.3$. Sauvage et al. (1990) analyzed the LMC extended emission using *Infrared Astronomical Satellite* (*IRAS*) data and noticed that regions with high I_{60}/I_{100} and low I_{12}/I_{25} correspond to star-forming regions. They concluded that the decrease in I_{12}/I_{25} was due to a lack of PAH emission, which dominates in the 12 μm band, and is now seen to be characteristic of low-metallicity environments. Sakon et al. (2006) analyzed the DIRBE data toward the LMC. They found that dust in the LMC is generally significantly warmer (in the range 21–27 K) than in the MW. They noticed the existence of some DIRBE pixels which are unusually bright at 240 μm, in particular in the surrounding of H I Super Giant Shell SGS11 (see Kim et al. 2003), but are also distributed somewhat more randomly within the LMC. They interpreted these pixels as the presence of cold dust ($T < 9$ K). Comparing the emission in excess to the FIR

emission in the DIRBE bands at 12, 25, and 60 μm with that for the inner regions of the MW, they showed that the LMC has proportionally less 12 μm and 25 μm and more 60 μm emission than the MW. They interpreted this as an indication that the size spectrum of small particles is different in both galaxies with the LMC having a distribution skewed toward larger particles. However, they noticed that because of the uncertainties in modeling the FIR component, in particular their working hypothesis of a single dust temperature and spectral emissivity index over a DIRBE pixel, the conclusion at 60 μm may be only marginal. Note that their results about the size distribution required are in apparent contradiction with the results on more distant low-metallicity galaxies by Galliano et al. (2005), which may indicate less extreme size distribution variations in the case of the LMC.

At FIR wavelengths, *IRAS* observations have revealed that the peak of the emission associated with H II regions is located around ~60 μm, corresponding to a temperature for the Big Grains (BG) of $T \sim 30$ K (DeGioia-Eastwood 1992). However, lower or higher temperature, depending on the evolutionary stage of the H II region, will move the peak at longer/shorter wavelengths, as observed by Peeters et al. (2002) for Galactic H II regions. Focused studies of H II regions in the LMC also have been carried out with the *Infrared Space Observatory* (*ISO*) (e.g., Vermeij et al. 2002; Li & Draine 2002; Madden et al. 2006, which also found PAH abundances lower in the LMC than in the MW). Vermeij et al. (2002) found clear correlations between the relative strengths of PAH features, such as $I_{7.7}/I_{11.2}$ and $I_{8.6}/I_{11.2}$ with respect to $I_{6.2}/I_{11.2}$. These correlations appear to follow a sequence from MW values with high-ratio to low-metallicity environments such as LMC and SMC with low ratios, a trend similar to that of the strength of the UV bump, indicating that some link may exist between the PAH emission and the 2200 Å bump. Within the LMC, Vermeij et al. (2002) noticed a strong segregation of the feature ratios between the vicinity of 30 Dor and non-30 Dor environments, with 30 Dor exhibiting SMC-like colors and other regions being more MW-like. The authors interpreted their results as an effect of the molecular structure of the PAH molecules being more compact in the SMC and 30 Dor and more open and uneven in the rest of the LMC and the MW. Vermeij et al. (2002) also reported no evidence of PAH abundance variations in their sample of H II regions.

Previous studies of the ISM in the LMC have suffered from the lack of angular resolution of the FIR data (e.g., DIRBE, FIRAS) and/or the lack of spatial and wavelength coverage (e.g., *ISO*). The availability of the *Spitzer* SAGE data now opens the possibility of carrying out large-scale studies of the dust emission in the LMC on much firmer grounds. In particular, the angular resolution of the SAGE data (from about 2″ at 3.6 μm to 40″ at 160 μm) now allows one to separate the extended emission from the stellar contribution, which is dominant in the NIR, in order to reveal the structure of the extended emission in the NIR, to perform spatial correlations of the emission with gas tracers in order to separate the contribution from the various phases of the ISM, and to derive the FIR dust properties, such as the equilibrium temperature of the largest grains (and therefore the radiation field intensity) at the *IRAS* scale of a few arcminutes (instead of 40′ with DIRBE FIR bands). This is an important improvement since, judging from the sizes of nearby MW Giant Molecular Clouds (GMCs), the resolution of a few arcminutes corresponds to the expected size of GMCs with a mass of a few $10^5 M_\odot$ at the distance of the LMC.

The goal of this paper is to explore and exemplify such studies using the SAGE data. We first describe the SAGE IR data in Section 2, focusing on the features that are important in the framework of analyzing the extended emission. We also present (in Section 3) the ancillary data that we use for such studies, in order to trace the gas distributions in the LMC. In Section 4, we describe the additional data processing performed on both the SAGE and ancillary data that is specific to the study of the extended emission presented in this paper, as well as the dust model used in the analysis. In Section 5, we compare the SED of the integrated LMC ISM emission with a reference SED of the MW plane and the integrated SED of the SMC, in the wavelength range from 3.6 μm to 500 μm. We show evidence for the existence of an MIR excess emission near 70 μm. In Section 6, we construct temperature and optical depth maps of the LMC using the FIR data and show evidence for the existence of a FIR excess emission with respect to gas tracers. In Section 7, we select a few representative regions of the LMC and derive the SED of the dust associated with the neutral and molecular phases of the ISM for these regions. In Section 8 we describe the procedure used to fit all SEDs analyzed in this paper and discuss the quality of the fits. In Section 9 we discuss the results in terms of the dust abundance and composition in the various phases of the ISM, both for the global analysis and for the selected regions. Section 10 is devoted to conclusions.

2. SAGE OBSERVATIONS

The infrared images were generated as part of the SAGE project (see Meixner et al. 2006), using the imaging instruments on the *Spitzer Space Telescope* (Werner et al. 2004). The Infrared Array Camera (IRAC) generates images in four MIR wavebands with central wavelengths 3.6, 4.5, 5.8, and 8 μm (Fazio et al. 2004). The Multiband Imaging Photometer for *Spitzer* (MIPS) generates images in three FIR wavebands: 24, 70, and 160 μm (Rieke et al. 2004). The observing strategy and data analysis procedures are described by Meixner et al. (2006).

Figures 1–4 show the overall *Spitzer* IR emission of the LMC at 160, 24, 8, and 3.6 μm. The IR emission is overlaid on the H I and CO integrated intensity contours. The positions of the areas studied in more detail in this paper are shown by the squares. It can be seen that the distribution of the FIR emission closely follows that of H I. Slight departures from the overall correlation are apparent in Figure 1, which can be interpreted as the existence of molecular material, or attributed to some variations of the temperature. At the shortest wavelengths, the emission is dominated by stellar emission mostly concentrated in the stellar bar.

Among the most relevant contributors to the observed IR emission are discrete H II regions. In particular, the LMC hosts the 30 Doradus complex, the brightest H II region in the Local Group which is thought to account for about 20% of the total FIR emission of the LMC (Aguirre et al. 2003). An accurate estimate of the H II regions' contribution to the total emission of the LMC is made complicated by the large variations in the physical properties (evolutionary stage, radiation field, etc.) of different objects as well as by crowding of the sources. In addition, understanding the dust emission in H II regions is generally made complicated by the uncertainties on the rapidly changing physical conditions within any given object. Such estimates and detailed studies are therefore beyond the goals of the present analysis and will be investigated in a forthcoming paper dedicated to H II region emission in the SAGE data.

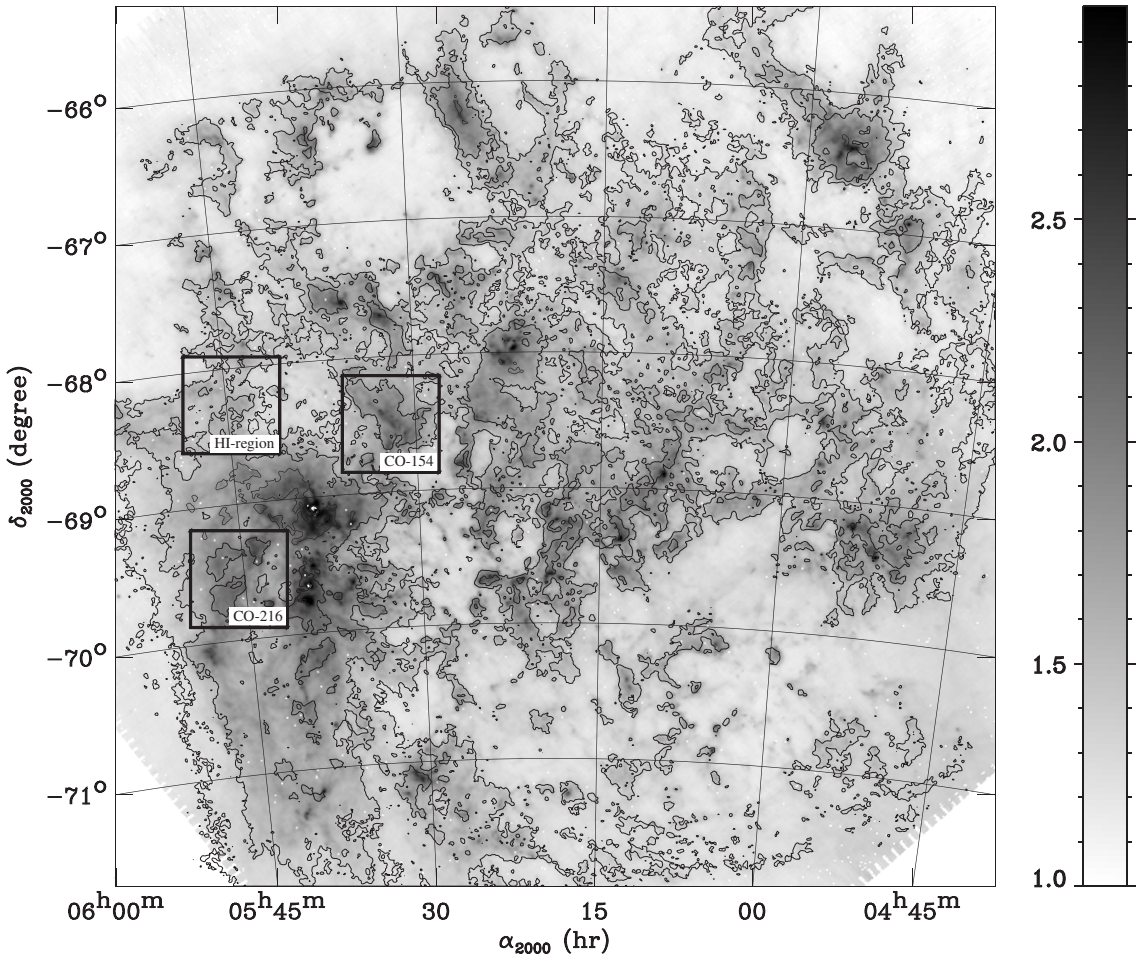

Figure 1. The SAGE map of the full LMC at 160 μm, overlaid with the H I integrated intensity contours at 0.7, 1.4, and 2.8 $\times$ 10^3 K km s^{-1} (corresponding to H I column densities of 1.2, 2.4, and 4.8 $\times$ 10^{21} H cm^{-2} respectively). The gray scale is $\log_{10}(I_\nu(\mathrm{MJy\ sr^{-1}})^{-1})$. The squares show the positions of the H I region (north-east region) and the CO regions (CO-154: north-west area, CO-216: south-east area) analyzed in Section 7.

3. ANCILLARY DATA

In order to correlate the dust emission properties with the gas emission, we use the ancillary datasets described below.

3.1. H I Emission

To trace the atomic gas, we use the H I map of the LMC obtained by Kim et al. (2003), combining data from the Australia Telescope Compact Array (ATCA) interferometer (Kim et al. 2003) and Parkes single-dish telescope (Staveley-Smith et al. 2003) covering 11.1° $\times$ 12.4° on the sky. The spatial resolution of the data available is 1′ corresponding to a physical resolution of ∼14.5 pc at the distance of the LMC. The coverage of the heliocentric velocity is $-33 < v_{\rm hel} < 627$ km s^{-1} with a velocity resolution of 1.649 km s^{-1}. The root mean square (rms) noise level of the final cube is 2.5 K. The large-scale H I distribution is characterized by a spiral structure which, with respect to optical images, does not present a bar. The most prominent concentration of H I is found in correspondence of the 30 Dor complex and extends 2° south. On small scales, the distribution is dominated by a complex system of filaments, shells, and holes. Kim et al. (1999) have identified 23 supergiant shells and 103 giant shells, and most of these appear to be correlated with similar structures observed in H_α.

We integrated in the H I data cube over the range $190 < v_{\rm hel} < 386$ km s^{-1} to construct the integrated intensity map, $W_{\rm H\,I}$. The integrated intensity map was transformed to K km s^{-1} units using (L. Staveley-Smith 2006, private communication).

$$\frac{W_{\rm H\,I}}{\rm K\,km\,s^{-1}} = 168.3 \times \frac{W_{\rm H\,I}}{\rm mJy/beam\,km\,s^{-1}}. \quad (1)$$

In the limit where the 21 cm line is optically thin, the column density is

$$\frac{N_{\rm H}^{\rm H\,I,thin}}{\rm H\,cm^{-2}} = 1.82 \times 10^{18} \frac{W_{\rm H\,I}}{\rm K\,km\,s^{-1}}. \quad (2)$$

In fact it is known that the 21 cm line in the LMC is at least moderately optically thick, based on the absorption spectra of background radio continuum sources (Marx-Zimmer et al. 2000). Half of the 20 radio sources had some 21 cm line absorption, with optical depths of 0.5 being not uncommon. These radio sources are not completely randomly distributed, being biased toward 30 Dor, the LMC 4 supergiant shell, and the H I "edge," E, of 30 Dor. The correction to the column density for optical depth effects is

$$\frac{N_{\rm H}^{\rm H\,I}}{N_{\rm H}^{\rm H\,I,thin}} = \frac{\int T_b \tau (1 - e^{-\tau})^{-1}\, dv}{\int T_b dv}, \quad (3)$$

where v is the velocity and T_b is the brightness temperature. We do not know the optical depth at each velocity and position for the LMC. We know only the observed brightness temperature.

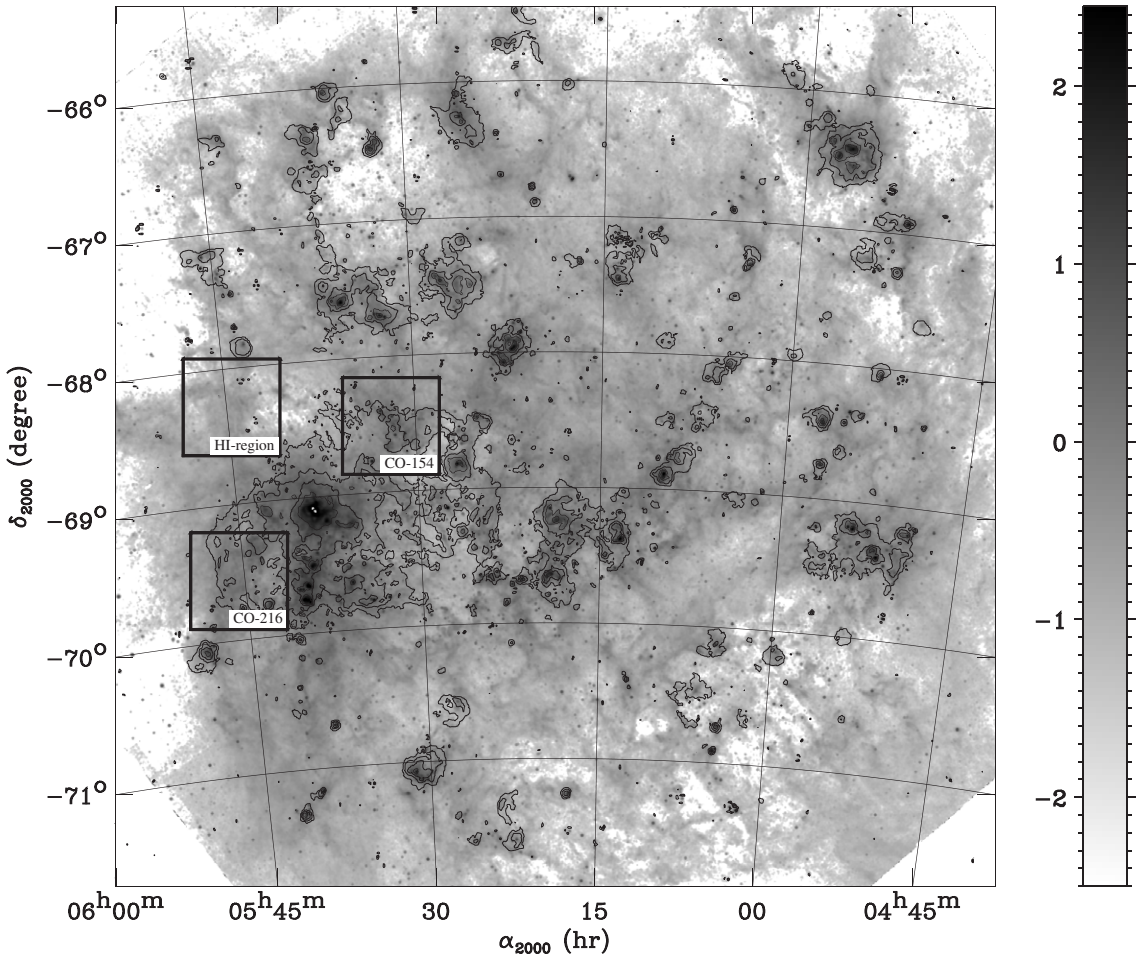

Figure 2. The SAGE map of the full LMC at 24 μm, overlaid with the H_α emission with contours at 40, 120, 360, and 1080 Rayleighs. The gray scale is $\log_{10}(I_\nu(\mathrm{MJy\,sr^{-1}})^{-1})$. The squares show the positions of the selected regions (see Figure 1).

For gas with a single spin temperature T_s, the brightness temperature is $T_b = T_s(1 - e^{-\tau})$. If we assume T_s, then we can infer the optical depth from the observed brightness and calculate the corrected column densities. If the emission arises from warm gas (i.e, with temperature being $T_s > 200$ K) then the 21 cm line is always optically thin, since the maximum observed brightness temperature is only 140 K. But 21 cm absorption studies in the MW find cold atomic gas temperatures of 60 K, and in the LMC the cold atomic gas is either much colder ($T_s \simeq 30$ K) or much more abundant (Marx-Zimmer et al. 2000). We therefore must anticipate some optical depth effects in the 21 cm observations of the LMC, possibly at a level more severe than the MW and the SMC (Dickey et al 2000). To illustrate the effect of cold, optically thick atomic gas, we assume $T_s =$ 60 K, solve for the optical depth at each velocity, and recompute the column density at each pixel, $N_{\rm H}^{{\rm H\,I},T_s=60}$. In regions of low-column density, the brightness temperature is low enough such that the 21 cm line is optically thin. However, toward most of the regions with a noticeable structure, at $N_{\rm H}^{\rm H\,I,thin} > 10^{21}$ cm^{-2}, the column density is increased significantly. The total H I mass of the LMC, assuming that the 21 cm line is optically thin everywhere, is $4 \times 10^8 M_\odot$, while using the $T_s =$ 60 K assumption, the total H I mass is 3.3 times larger. The column density correction factor

$$f_{T_s=60} = \frac{N_{\rm H}^{{\rm H\,I},T_s=60}}{N_{\rm H}^{\rm H\,I,thin}} \quad (4)$$

ranges from 1 to 8 over nearly all of the LMC, with a median of 1.2. For $N_{\rm H}^{\rm H\,I,thin} = 10^{21}$ and 2×10^{21} H cm^{-2}, typical of the lines of sight where we could measure the dust temperature with the *Spitzer* data, the median correction $f_{T_s=60} = 1.3$ and 3.9, respectively. In these regions, we expect the column density inferred assuming that the 21 cm line is optically thin to be too low by these factors.

The LMC, being located at galactic latitude $b = -34°$, is subject to significant contamination by galactic foreground emission which has to be removed from the IR data. In order to account for the galactic foreground toward the LMC, we used a galactic H I column density map constructed by Staveley-Smith et al. (2003) by integrating the Parkes H I data in the velocity range from $-64 < v_{\rm hel} < 100$ km s^{-1}, which excludes all LMC-associated gas ($v > 100$ km s^{-1}) but includes essentially all galactic emission. This map shows that the galactic foreground across the LMC is as strong as $N_{\rm H} = 1.3 \times 10^{21}$ H cm^{-2}, with significant variation across the LMC, in particular a wide filamentary structure oriented SW to NE. We use the optically thin limit for the galactic H I in front of the LMC, assuming that most of the 21 cm line emission on these lines of sight is from warm gas or diffuse cold gas. This foreground map was used to subtract the foreground IR emission from the IR maps, using the solar neighborhood SED described in Section 5.2. The lack of galactic-velocity CO shows that there are no strong condensations of galactic ISM toward the LMC. The average corresponding extinction over the LMC extent is

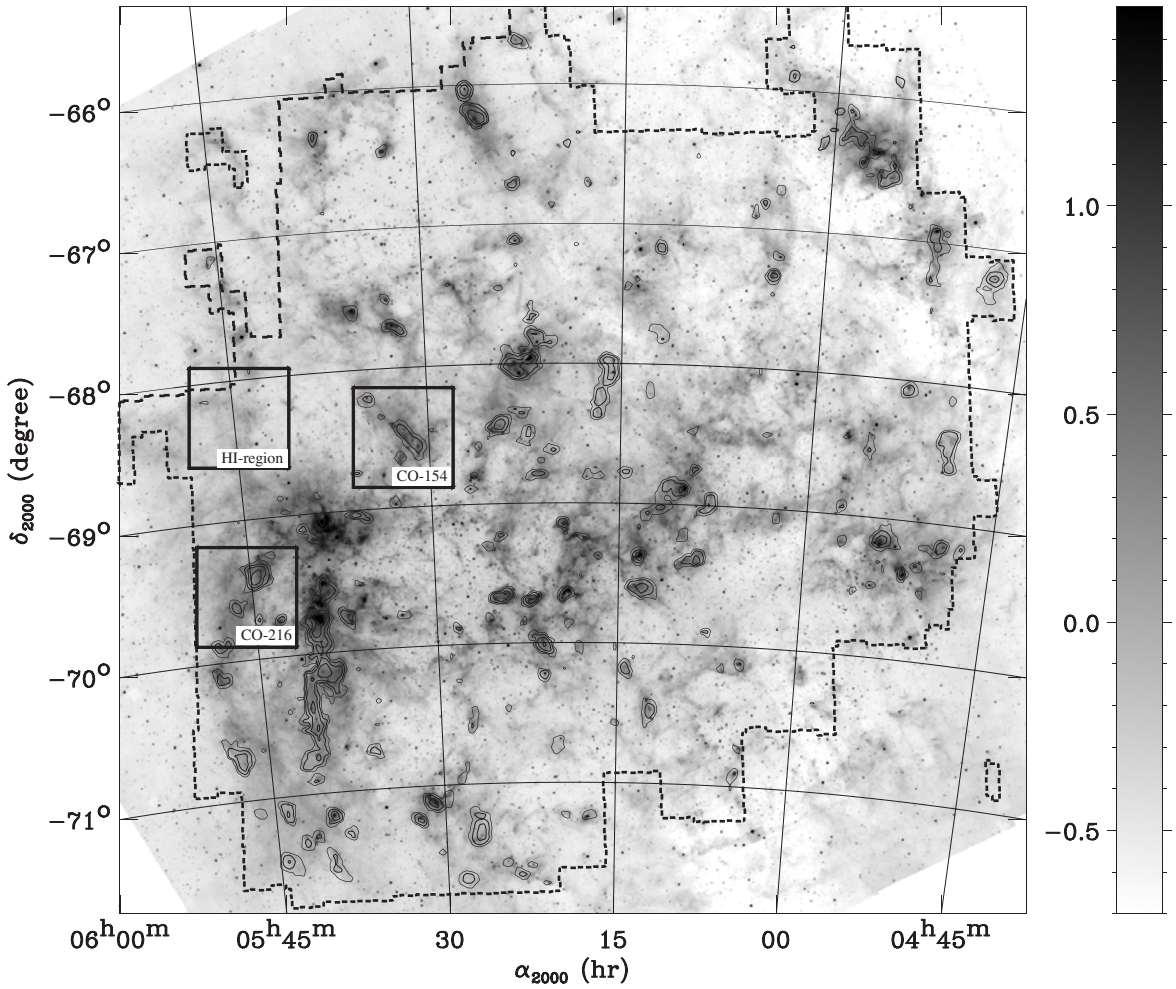

Figure 3. The SAGE map of the full LMC at 8 μm, overlaid with the NANTEN ^{12}CO($J = 1 - 0$) integrated intensity contours at 1, 2, 4, and 8 K km s^{-1}. The dashed contours shows the limits of the NANTEN survey. The gray scale is $\log_{10}(I_\nu(\mathrm{MJy\,sr^{-1}})^{-1})$. The squares show the positions of the selected regions (see Figure 1).

about $E_{B-V} \simeq 0.06$ corresponding to $Av \simeq 0.2$ mag assuming a ratio of total to selective extinction $Rv = 3.1$.

3.2. CO Emission

The CO ($J = 1$–0) molecular data used in this work were obtained using the NANTEN telescope, a 4 m radio telescope of Nagoya University at Las Campanas Observatory, Chile (see Fukui et al. 2008). The observed region covers about 30 deg^2 where CO clouds were detected in the NANTEN first survey (e.g., Fukui et al. 1999; Mizuno et al. 2001). The observed grid spacing was 2′, corresponding to about 30 pc at a distance from the LMC, while the half-power beam width was 2.6′ at 115 GHz. The typical $3 - \sigma$ noise level of the velocity-integrated intensity is about 1.2 K km s^{-1}. This corresponds to $N(\mathrm{H_2}) = 8 \times 10^{20}$ cm^{-2}, using a CO-to-H$_2$ conversion factor of $X_{\mathrm{CO}} = 7 \times 10^{20}\,\mathrm{H_2\ cm^{-2}\ (K\ km\ s^{-1})^{-1}}$. The total mass of the molecular gas in the LMC is about $5 \times 10^7\,M_\odot$ using the same X_{CO} factor, which is about ten times less than the H I mass derived under the assumption of thin H I emission. The CO distribution of the LMC is found to be clumpy with some large MC complexes, contrary to the filamentary and shell-like structures of H I gas distribution. Fukui et al. (2008) identified 272 MCs, about 1/4 of which were associated with optically identified young clusters by Bica et al. (1996) (Type III), about half with optically identified H II regions (Type II), and the rest not associated with any indicator of massive star formation in optical data (Type I).

We used the CO map to construct an integrated intensity map (W_{CO}), integrating over the full v_{lsr} range of the data ($100 < v_{lsr} < 400\,\mathrm{km\,s^{-1}}$ for about 80% of the data, while 20% had a velocity range of about 100 km s^{-1} covering the H I emitting regions).

In this paper, we derived molecular column densities using

$$\frac{N_{\mathrm{H}}^{\mathrm{CO}}}{\mathrm{H\,cm^{-2}}} = 2X_{\mathrm{CO}} \times \frac{W_{\mathrm{CO}}}{\mathrm{K\,km\,s^{-1}}}, \quad (5)$$

and assuming the average X_{CO} factor derived from the Virial analysis of the CO emission in Fukui et al. (2008), $X_{\mathrm{CO}} = 7 \times 10^{20}\,\mathrm{H_2\ cm^{-2}\ (K\ km\ s^{-1})^{-1}}$.

3.3. H_α Emission

The ionized gas component is taken into account through H_α emission with the Southern H Alpha Sky Survey Atlas (SHASSA, Gaustad et al. 2001), covering the southern sky with a field of view of 13°. The survey has been carried out with a narrow-band imaging system consisting of an H_α filter of 3.2 nm bandwidth and a dual-band notch filter that excludes H_α but transmits a 6.1 nm band of continuum radiation on either side of H_α, centered at 644 and 677 nm. For the

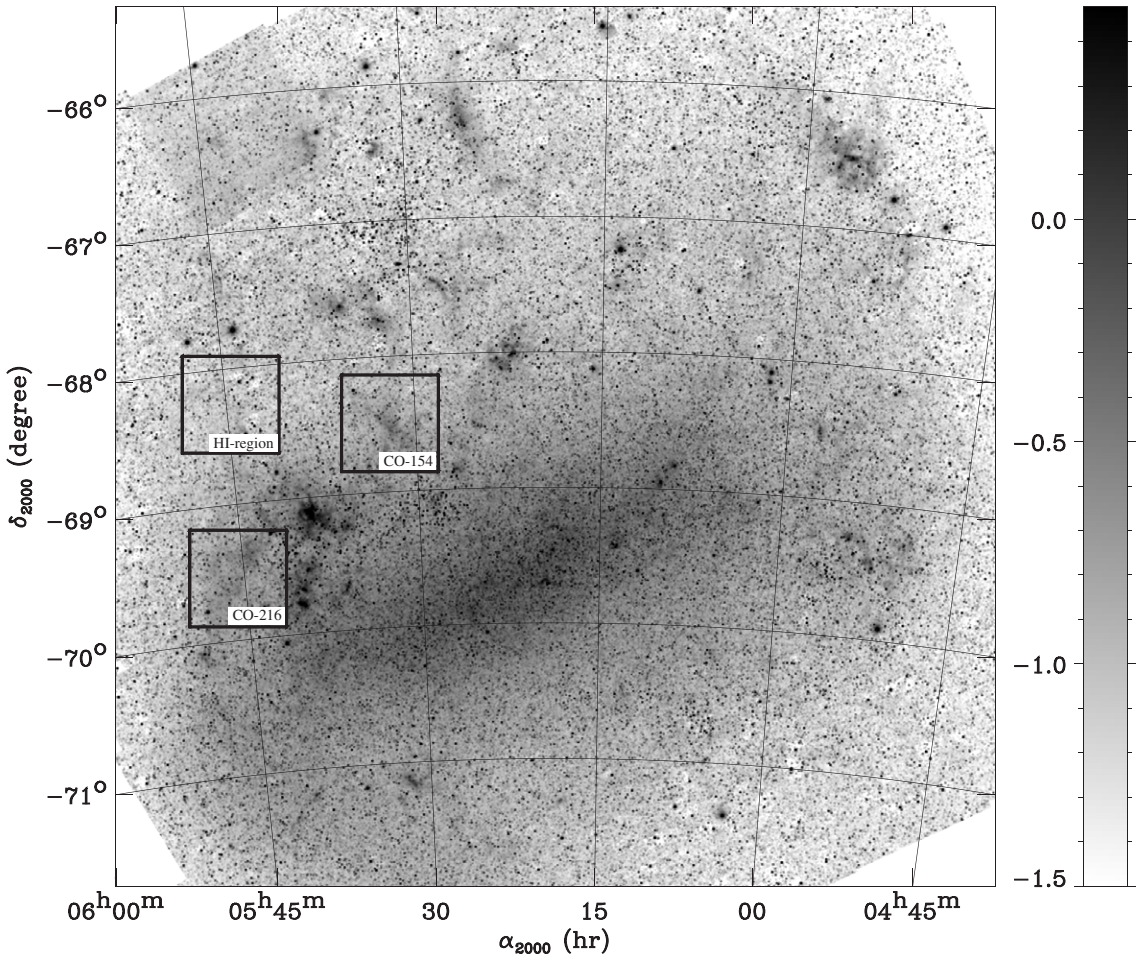

Figure 4. The SAGE map of the full LMC at 3.6 μm. The gray scale is $\log_{10}(I_\nu(\mathrm{MJy\,sr^{-1}})^{-1})$. The squares show the positions of the selected regions (see Figure 1).

analysis presented here, the continuum-subtracted map has been used. The survey angular resolution is 0.8′, which corresponds to a linear resolution of 11.6 pc. The sensitivity reaches 2 Rayleighs (1 Rayleigh = 10^6 photons cm^{-2} s^{-1} corresponding to 2.41 × 10^{-7} erg s^{-1} cm^{-2}) and it is mainly limited by geocoronal contamination. In fact, with respect to Fabry–Perot surveys, narrowband imaging observations do not provide velocity information and therefore do not allow separation of the interstellar H_α with respect to the Earth' geocorona.

The intensity map was transformed into electron column density using the relation

$$\frac{N_{\mathrm{H}}^{\mathrm{H^+}}}{\mathrm{H\,cm^{-2}}} = 1.37 \times 10^{18} \frac{I_{\mathrm{H}_\alpha}}{R} \left(\frac{n_e}{\mathrm{cm^{-3}}}\right)^{-1} \quad (6)$$

given the assumption that 1 Rayleigh corresponds to an emission measure of 2.25 cm^{-6} pc, assuming a gas temperature of T_e = 8000 K (see, for instance, Dickinson et al. 2003). Note that the above relation is valid only where a constant density can be assumed, which is probably an acceptable approximation in the diffuse ionized medium, but would lead to erroneous results where large values of I_{H_α} are observed. In the present analysis, we use it only at low emission measures (H_α < 200 R). Also note that no correction for extinction in the H_α data is applied in the present analysis.

4. DATA HANDLING

In addition to the processing of the SAGE data presented in Meixner et al. (2006), the following treatment, necessary to the analysis of the extended emission, was applied to the SAGE maps.

4.1. Point Source Blanking

At IRAC frequencies, pixels affected by stellar emission were removed by blanking a circular region around each star detected in the SAGE point-source catalog (we used Epoch1+2 catalog 20060511), with a diameter ϕ_{blank} proportional to the flux source F, using

$$\phi^2_{\mathrm{blank}} = \left(\ln\left(\frac{F}{\Omega}\right) - \ln(B_l)\right) \frac{\theta^2_{\mathrm{FWHM}}}{ln(2)}, \quad (7)$$

where θ_{FWHM} is the point-spread function (PSF) full width at half-maximum (FWHM) size, F is the point source flux in Jy, B_l is the threshold brightness, and Ω is the PSF solid angle $\left(\Omega = \pi\theta^2_{\mathrm{FWHM}}\right)$. For the faintest sources for which Equation (7) leads to masking less than 1 pixel of the image, the mask is set to 1 pixel. The parameters used for the various *Spitzer* channels are given in Table 1.

Although the above procedure masks most stars, a few bright point sources remain that are not well accounted for in the catalog. These are identified using two successive calls to the DAOPHOT "find" procedure with a detection threshold set to 500 − σ for the brightest sources and then a detection threshold set to 30 − σ for the remaining sources, where σ is the image rms in an empty region. Sources found in this way are also masked using Equation (7) but using a value of ln(B_l) 40 times

Table 1
Parameters Used for Star Masking

Band	$\ln(B_l)$ (MJy sr^{-1})	$\theta_{\rm FWHM}$ ($''$)
IRAC 3.6	−6.95	4.72
IRAC 4.5	−7.29	4.76
IRAC 5.8	−4.21	5.31
IRAC 8.0	−5.03	5.61
MIPS 24	−3.12	6.00
MIPS 70	0.053	18.0
MIPS 160	2.88	40.0

larger than given in Table 1 for the brightest sources (detected at $500-\sigma$).

4.2. Photometry Correction for Extended Sources

IRAC was calibrated for a finite aperture; for this paper we are interested only in the extended emission so we correct the images by multiplying by empirically-derived factors 0.944, 0.937, 0.772, and 0.737 to account for light lost from the stellar calibration aperture (Reach et al. 2005).

4.3. Convolution to Common Resolution

All maps were convolved to a common resolution σ_c through convolution by a Gaussian kernel with FWHM $\sigma_k^2 = \sigma_c^2 - \sigma_d^2$, where σ_d is the original resolution of the maps. Masks identifying the pixels of the original images, which were blanked due to PS subtraction were also convolved in the same way, and processed as the rest of the data. They are used at weighting the data in the correlation analysis presented in Section 8. Note that these masks are also applied to non-SAGE data such as infrared interferometer spectrometer (IRIS) images used in the study (we used the 8, 24, 70 and 70 μm masks for the IRIS 12, 25, 60, and 100 μm bands respectively), in order to penalize IRIS pixels affected by significant contribution from point sources in the correlations.

In this paper, we use essentially data at the resolution of the *IRAS* 100 μm band, i.e., $\sigma_c = 4'$, since combining the *IRAS* and *Spitzer* datasets is required for an accurate determination of the dust temperature. We also use $\sigma_c = 1'$ in some of the analysis presented here, for instance in Section 5.3.

All images were then regrided to a common FITS pixelization, using standard WCS routines. A similar procedure was applied to all data used, including the *IRAS* and ancillary data, when the resolution of the ancillary data was higher than the common resolution.

4.4. Foreground and Background Subtraction

The IR foreground contribution at all *Spitzer*/*IRAS* frequencies was subtracted from the map using the H I foreground map described in Section 3.1. This contribution has been evaluated using the IR emissivity values corresponding to the best fit of the average high latitude galactic mission SED of Dwek et al. (1997) (see Section 5.2). Note that the resolution of the H I foreground map is $14'$, significantly lower than the resolution used in the present study, $(4'-1')$ but smaller than the size of the correlation boxes selected around each region in the LMC (0.7°). One must therefore keep in mind that residual emission structures at the scale below $14'$ in the present analysis could be due to residual contribution from the galactic foreground.

Estimates of the level of the zodiacal light emission have been subtracted from the IRAC maps and from the MIPS maps at 24 μm in the SAGE pipeline. However, arbitrary offsets may subsist in the maps which need to be removed before large-scale emission can be analyzed quantitatively. In order to subtract any contribution from residual-extended emission such as zodiacal light, cosmic IR background, or artifact offset in the data, all images were background subtracted by removing the 10% lower percentile value computed in a region common to all images, away from the main emitting regions of the LMC. The common background region is defined such that $N_H^{HI} < 1.5 \times 10^{20}$ H cm^{-2}. A similar procedure was applied to all data used.

4.5. Dust Emission Model

In order to explain the IR observations, we use the dust emission model proposed by Désert et al. (1990). This model fully takes into account stochastic heating of very small grains (VSG). It invokes three dust populations: PAH, VSG assumed to be mainly composed of carbonaceous material, and big dust grains (BG) composed of silicate. The original model was updated to account for the actual shape of the PAH emission features as derived from ISO and *Spitzer* Spectroscopy measurements and to include the 17 μm feature attributed to PAH. We also added an NIR continuum (with a temperature T=1000 K), which was originally detected in reflection nebulae (Sellgren et al. 1983) and whose existence was later found both in the MW from DIRBE (Bernard et al. 1994) and *Spitzer* data (Flagey et al. 2006) and in external galaxies (Lu et al. 2003, 2004). The same assumptions as in Flagey et al. (2006) are used in the model regarding the contribution of PAH with various ionization stages. Although we do not fit for the ionization fraction of PAH, we tried several ionization fractions and concluded that the data are compatible with a fully neutral population of PAH for the regions included in this paper. This is consistent with the fact that the radiation field intensities sampled in the selected regions are moderate.

The model was interfaced so that emission can be computed in the photometric channels of the instruments used here (*IRAS*, DIRBE, IRAC, MIPS) when necessary, taking into account the color corrections, using the actual transmission profiles for each instrument, and following the flux convention description given in the respective explanatory supplements. The model was further interfaced with a minimization tool allowing automated fits of SED combining measurements from these instruments, as well as narrow band or spectral data (such as FIRAS). Use of the model in this context is described in Section 8.

5. LMC EMISSION COMPARED TO THE MW AND SMC

In this section, we construct the SED of the integrated emission of the LMC and compare it with that of the SMC and the MW plane. The goal is to place the LMC in context, in order to compare with other galaxies, and also to perform a large-scale calibration check of the SAGE data with respect to other IR data of the LMC. The global SEDs derived in this section are also used in the rest of this paper (see Section 8), as a reference to compare the individual SEDs derived from selected individual regions in the LMC with its total emission and the MW emission.

5.1. Overall SED of the LMC

We constructed the total SED of the LMC merging the *Spitzer* SAGE data with the Improved Reprocessing of the *IRAS* data (IRIS: Miville-Deschênes & Lagache 2005) and the FIRAS data. The total SAGE fluxes were computed using the maps processed

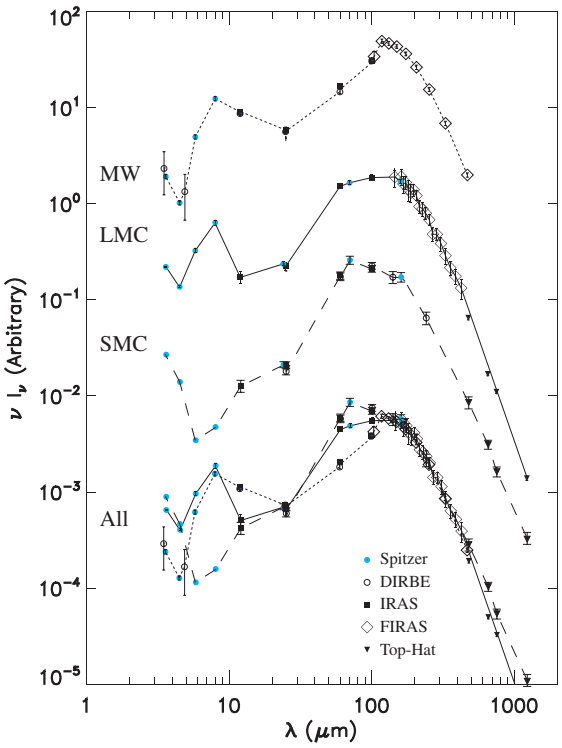

Figure 5. The SED of the entire LMC (solid) compared to the MW plane SED (short dash) and the SMC SED (long dash). The lower curves show the same SEDs normalized in the FIR. The *Spitzer*, DIRBE, *IRAS*, FIRAS, and top-hat data are shown by the filled circles, open circles, filled squares, open diamonds, and downward triangles respectively. The SMC SED is from Leroy et al. (2007) for the *IRAS* and MIPS data points, from Stanimirovic et al. (2000) for the DIRBE points, and from Bolatto et al. (2007) for the IRAC points. The MW plane SED is discussed in Section 5.2. The LMC SED is discussed in Section 5.1. All SEDs have the contribution from point sources subtracted (see text for details). All error bars are $\pm 1 - \sigma$.

(A color version of this figure is available in the online journal.)

as described in Section 4. We summed all values in the *Spitzer* SAGE images. The FIRAS and IRIS data were averaged in a circular region with diameter 8° centered on the LMC, with a surrounding background region of radius 16°. The error bars were derived from the data error, and also include the uncertainty due to background subtraction, derived from the dispersion of brightness values in the background region defined in Section 4.4. The resulting SED is shown in Figure 5. FIRAS data with the lowest signal-to-noise ratio (S/N) have been omitted for clarity. In the sub-millimeter, the levels obtained are consistent with the measurements from the top-hat experiment (see Aguirre et al. 2003).

The comparison between the SAGE data at MIPS wavelengths (24 μm, 70 μm, and 160 μm) and the IRIS data at 25 and 60 μm and the FIRAS data shows a good agreement, indicating that the overall calibration of the SAGE data is accurate within the error of the available data. The largest apparent difference is between the MIPS 24 μm and *IRAS* 25 μm channels, where the difference between the two measurements is about 10%, but remains within the $3 - \sigma$ uncertainties of the *IRAS* measurement. Engelbracht et al. (2007) found a similar result, but also found the offset to be well within the scatter observed in a much larger sample of galaxies. Note that a detailed comparison between the IRAC and DIRBE photometry in the 3.5 and 4.9 μm DIRBE channels cannot be easily performed because of the difficulty of removing the stellar contribution from the background region around the LMC in the DIRBE data.

We then derive the total contribution from the ISM emission by subtracting the point-source contribution. We computed the contribution from point sources to the total LMC SED, by subtracting from each *Spitzer* band the integrated flux in the IRAC[23] and MIPS[24] point-source catalogs generated using the SAGE pipeline. At DIRBE and *IRAS* wavelengths, a similar correction was applied by interpolating into the values at *Spitzer* wavelengths. For the FIRAS part of the spectrum, point sources were assumed to contribute the same fraction of the total flux at 160 μm. Note that point sources dominate the total LMC emission in the IRAC 3.6 and 4.5 μm bands, and become about 50% and lower at 8 μm and above. The values for the extended emission SEDs were further corrected for the PS/extended emission correction factors for IRAC given in Section 2. The resulting global SED of the LMC is compared to that of the MW and the SMC in Figure 5. The SMC SED is from Leroy et al. (2007) for the *IRAS* and MIPS data points, from Stanimirovic et al. (2000) for the DIRBE points, and from Bolatto et al. (2007) for the IRAC points. Note that we used the total flux from table 3 of Bolatto et al. (2007), subtracted from the point-source contribution, also taken from this table. Also note that the IRAC photometric points were computed in regions that do not necessarily match those of the MIPS points.

For further analysis in this paper (see Section 8), the total LMC SED was normalized to the average total gas column density of the LMC. The average H I column density of the LMC was derived by averaging the background-subtracted H I integrated intensity data of Kim et al. (2003) within a radius of 6° from the center of the LMC, which encompasses most of the detected H I emission. The derived average column density is $N_{\rm H}^{\rm H\,I} = 6.3 \times 10^{20}$ H cm^{-2} under the assumption of thin H I emission, corresponding to a total H I mass of $M_{\rm H\,I} = 4.6 \times 10^8 M_\odot$. The column density contribution from CO was estimated using the total molecular mass derived by Fukui et al. (2008) of $M_{\rm CO} = 5 \times 10^7 M_\odot$, which corresponds to an average column density of $N_{\rm H}^{\rm CO} = 6.8 \times 10^{19}$ H cm^{-2} in the integration region. Note that this estimate takes into account the average value of the $X_{\rm CO}$ factor ($X_{\rm CO} = 7 \times 10^{20}$ H$_2$ cm^{-2} (K km s^{-1})$^{-1}$, used throughout this paper, see Section 3.2) and its variations derived from the Virial analysis of the NANTEN data. The total average column density derived is $N_{\rm H}^{\rm tot} = 7 \times 10^{20}$ H cm^{-2}. The corresponding SED will be described in Section 8.

5.2. Overall SED of the MW

Several attempts have been made to construct the global SED of the IR galactic emission. Bernard et al. (1994) used the early DIRBE data to construct the average SED over a set of clouds along the galactic plane. Boulanger et al. (1996) constructed the average FIRAS SED of high-latitude galactic material and derived an average SED consistent with dust at $T = 17.5$ K and a FIR spectral index $\beta = 2$. Dwek et al. (1997) constructed the average SED of the diffuse ISM from 3.5 μm to 1 mm, combining DIRBE and FIRAS data toward high-galactic-latitude regions, and found an SED very similar to that of Bernard et al. (1994) in the DIRBE range. Arendt et al. (1998) used the DIRBE all-sky data to produce the SED of the galactic emission from 1.25 μm to 240 μm. Note that each of these determinations was indeed obtained in different regions of the sky. The fact that these determinations agree reasonably

[23] IRAC: catalog epoch1+2+3.
[24] MIPS: epoch 1+2.

well in the NIR and MIR indicates that the shape of the SED does not vary greatly over this spectral range.

However, the above estimates were mainly dedicated to understanding dust properties in the diffuse high-galactic-latitude regions corresponding to the solar neighborhood and none of them is actually representative of the overall emission of the galactic plane, which spans a wide range of temperature and density. We therefore construct an average SED of the galactic plane by combining the IRIS, DIRBE, and FIRAS data. After being re-pixelized to the Healpix pixelization scheme,[25] all data were degraded to the resolution of the FIRAS data (7°) by convolution with the appropriate Gaussian kernel. A similar treatment was applied to the all-sky $N_{\rm H}$ map combining the Leiden/Dwingeloo (Hartmann & Burton 1995) and the Southern survey by Dickey & Lockman (1990), as provided on the lambda Web site.[26] We extracted the galactic SED by considering regions with $W_{\rm HI} > 500$ K km s^{-1} ($N_{\rm H} > 9.1 \times 10^{20}$ H cm^{-2}) and subtracting a background at all wavelengths in regions with $500 < W_{\rm HI} < 200$ K km s^{-1} ($3.6 \times 10^{20} < N_{\rm H} < 9.1 \times 10^{20}$ H cm^{-2}), in order to subtract any zodiacal light or Cosmic Infrared Background emission residual. The resulting MW SED will be discussed in Section 8.

In this paper, we use the SED derived by Dwek et al. (1997) to represent the solar neighborhood and the galactic plane SED described above for the galactic plane emission. They are called MW (Diff) and MW (Plane) respectively in the following.

5.3. 70 μm *Excess*

Figure 5 shows the comparison of the total SED of the MW, LMC, and SMC. In the lower part of the figure, the SEDs have been normalized in the FIR to better evidence the variations in their shape. It is clearly apparent on the normalized SEDs that an excess emission is present in the LMC and SMC SEDs at 60 and 70 μm, which could even affect the 100 μm point. It is also clear that the excess emission rises from the MW to the LMC and is maximum in the SMC. All three normalized SEDs match well at 25 μm and then split again at 12 μm, with this time the highest relative brightness for the MW and the lowest for the SMC, a reverse situation as compared to that in the 70 μm excess. As part of the *IRAS* 12 μm is produced by the dust emission continuum (the rest being contributed by the PAH features at 11.3 μm and 7.7 μm), this is likely to indicate a systematic steepening of the continuum SED in the MIR, with the MW having the flattest and the SMC the steepest SEDs respectively, and an intermediate slope for the LMC. This could reflect systematic changes in the size distribution of the small grains producing the MIR emission and/or modification of the interstellar radiation field (ISRF) strength. Also note that the SEDs of the MW and LMC match again in the *Spitzer* 8 μm bands. However, this could be somewhat fortuitous, since the *Spitzer*-IRAC values used here for the MW were not obtained in the exact same region as the other points of the MW SED. Indications for the existence of similar MIR excess emission were identified in the SMC (Bot et al. 2004), in the LMC (see Sauvage et al. 1990; Sakon et al. 2006), and even possibly toward unresolved galaxies (Galliano et al. 2003, 2005), although no spatial study of its distribution has been carried and no physical interpretation has been proposed.

[25] Hierarchical Equal Area isoLatitude Pixelization, see http://healpix.jpl.nasa.gov/.
[26] http://lambda.gsfc.nasa.gov.

In an attempt to assess the spatial distribution of the 70 μm excess, we used the following procedure to estimate the contribution from BG and VSG at 70 μm, using the dust emission model described in Section 4.5 and the standard parameters proposed by Désert et al. (1990). We first computed the *Spitzer* 160 μm to *IRAS* 100 μm ratio as a function of the ISRF intensity ($X_{\rm ISRF}$) using the model. This relation was fitted using a low-order polynomial and used along with the measured 160/100 ratio map to construct a map of $X_{\rm ISRF}$. Second, we used the model to compute the 24/70 ratio for VSG only and the 160/70 ratio for BG only as a function of $X_{\rm ISRF}$ and again fitted the corresponding relations using a low-order polynomial. Finally, we used the above relations with the measured 24 μm and 160 μm *Spitzer* emission maps and the $X_{\rm ISRF}$ map constructed above to estimate the contribution from BG and VSG to the 70 μm band and subtracted from the observed *Spitzer* map at 70 μm. The above method is based on the reasonable assumption that the observed emissions at 160 μm and 24 μm are dominated by emissions from BG and VSG respectively and fully takes into account the variation of the spectral shape of each component with the varying ISRF intensity. Note that since the method uses the *IRAS* 100 μm map to derive the ISRF strength, this is performed at the resolution of the *IRAS* data.

The spatial distribution of the 70 μm excess computed this way is shown in Figure 6. The figure shows that the 70 μm emission is extended in nature. Most regions of the LMC show a positive excess. However, the brightest excess regions concentrate in a 1° ring-shaped structure to the east and south of 30 Dor. Further spectral characterization and the possible interpretation of this excess emission will be discussed in Section 9.4.

6. FIR EMISSION DISTRIBUTION IN THE LMC

In this section, we derive an all-LMC map of the dust temperature and FIR optical depth. We use the 4′ resolution maps processed as described in Section 4.

6.1. Dust Temperature Map

We derive a map of the temperature of the BG in the LMC using the ratio of our *Spitzer* 160 μm and the IRIS image at 100 μm, assuming that the IR emission can be represented by a gray body emission

$$I_\nu \propto \nu^\beta B_\nu(T_d), \tag{8}$$

with $\beta = 2$ in the FIR. We used the *Spitzer* 160 μm map smoothed to the resolution of the IRIS map (4′). An iterative procedure was used to derive T_d along with the color corrections in the *Spitzer* and *IRAS* optical bands using the spectral shape of Equation (9). We estimated the error on the derived temperature using the uncertainties on 100 and 160 μm as measured by their standard deviations in the background region of each map (see Section 4). Pixels corresponding to low-emission regions obviously lead to larger errors. Those with errors in excess of 30% of the temperature value were removed from the final map.

Note that in past studies, such FIR-derived temperature maps could only be constructed at the resolution of the DIRBE data (1°). Also note that some of the past attempts at constraining the equilibrium temperature of the large grains in the LMC used the *IRAS* 60 μm emission. Emission at 60 μm is highly contaminated by out-of-equilibrium emission from VSG and this is even more so in the LMC, due to the presence of the 70 μm excess. Combining the *IRAS* 60 μm and 100 μm therefore

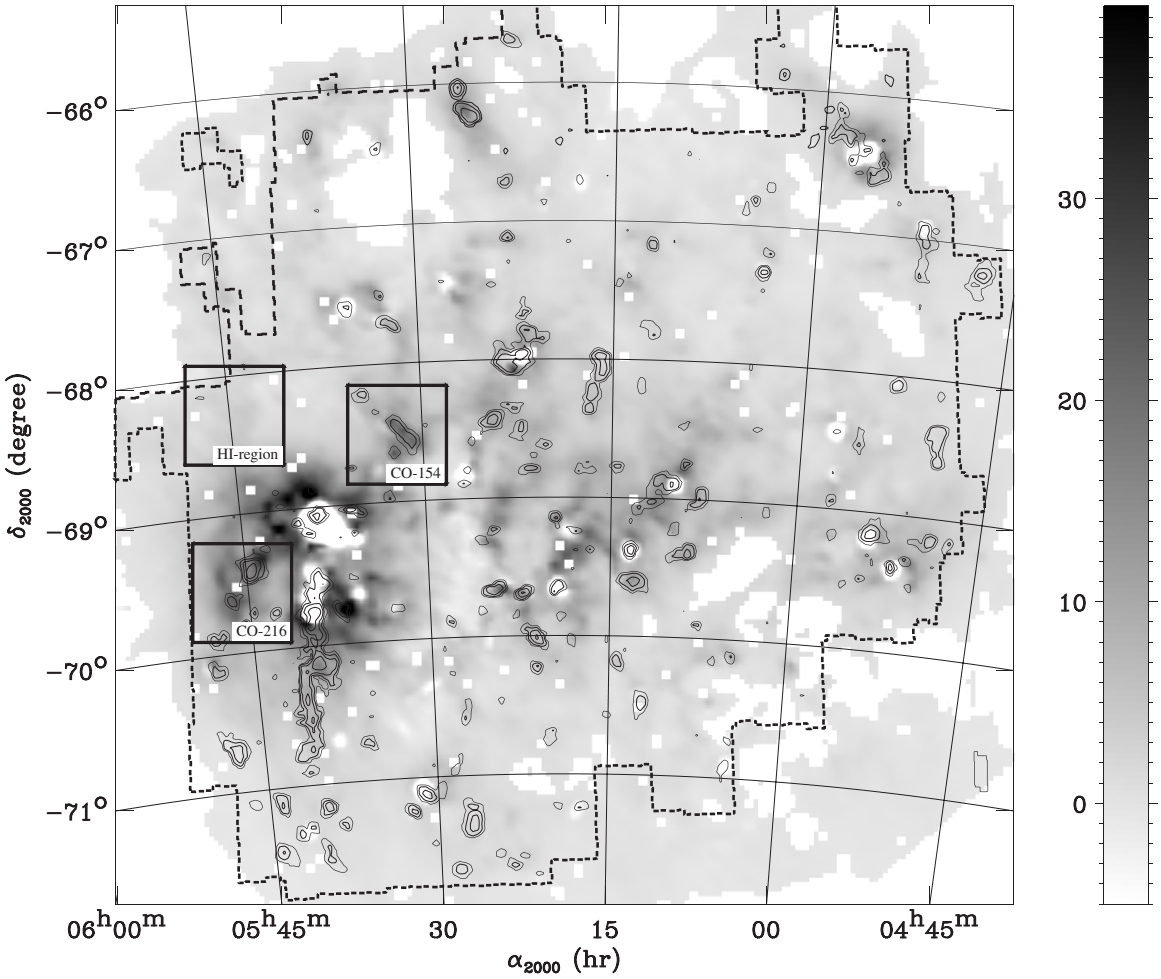

Figure 6. Spatial distribution of the 70 μm excess emission (gray scale) compared to the NANTEN ^{12}CO($J = 1 - 0$) integrated intensity contours (the same scale as in Figure 3). The gray scale is computed as described in Section 5.3 and shown in a linear scale in MJy sr^{-1}.

strongly over-estimates the temperature and accordingly under-estimates the abundances of all types of dust particles.

The temperature map derived is shown in Figure 7. Values of T_d vary from about 12 K to a maximum of 34.7 K at the location of 30 Dor. Formal relative errors on T_d are the highest near 12 K where they reach 30% and are much smaller at high T_d. The pixel ensemble median and mean values in the map at a resolution of 4′ are 18.3 K and 18.2 K respectively. As expected, this is significantly colder than previous determinations which included the MIR data in the estimate. For instance, the maps derived by Schwering (1989) and used in the analysis by Israel (1997) were warmer than 20 K over the same area as shown in Figure 7. Note that the average dust temperature derived here for the LMC indicates that the strength of the ISRF ($X_{\rm ISRF}$), which is related to dust temperature by $X_{\rm ISRF} \propto T^{4+\beta}$ for equilibrium emission, is only about 20% higher than in the solar neighborhood, where the dust is known to be at 17.5 K (using $\beta = 2$ Boulanger et al. 1996).

Our estimated median value (18.3 K) is lower than that derived from the FIR DIRBE data by Sakon et al. (2006), who found an ensemble median value of $\simeq$22 K for an assumed $\beta = 2$, judging from their Figure 4. We tested the influence of the angular resolution difference between the two datasets, by degrading the resolution of our maps to that of DIRBE ($\simeq$0.7°), and found a slightly higher median temperature of 19 K at that resolution, but still lower than their value. However, we note that the median value is very sensitive to the extent of the area used for the determination, and since temperatures decrease systematically toward the outer regions of the LMC, the residual difference between the two estimates could arise from Sakon et al. (2006) having selected a smaller region of the LMC, based on S/N considerations.

Aguirre et al. (2003) have derived temperatures of the LMC and 30 Dor region using the combination of the top-hat and DIRBE data at 100, 140, and 240 μm. Smoothing our maps to the resolution of the top-hat data (20′), integrating the flux over the LMC following their assumptions (excluding a 1.1° radius region around 30 Dor), and deriving the temperature as described earlier with their proposed $\beta = 1.33$, we obtain an apparent temperature of 21.4 K, which is significantly colder than their value (25 K $\pm$ 1.8 K). Similarly, we find an average 23 K for the 30 Dor region (using their $\beta = 1.50$), while they quote $T = 26.2$ K. However, we have checked that using their DIRBE flux values at 100 and 140 μm in our procedure, and taking into account the color correction in the DIRBE filters, lead to 23.4 K and 24.5 K respectively, much closer to our estimates. In addition, their fit systematically overestimates the *IRAS* 100 μm brightness (see their Figure 4). It is therefore likely that the apparent discrepancy resides in the use of data in the sub-millimeter, which will become available only at the resolution of our study with the *Herschel* satellite. The discrepancy could reflect uncertainties in the relative calibration of *IRAS* and

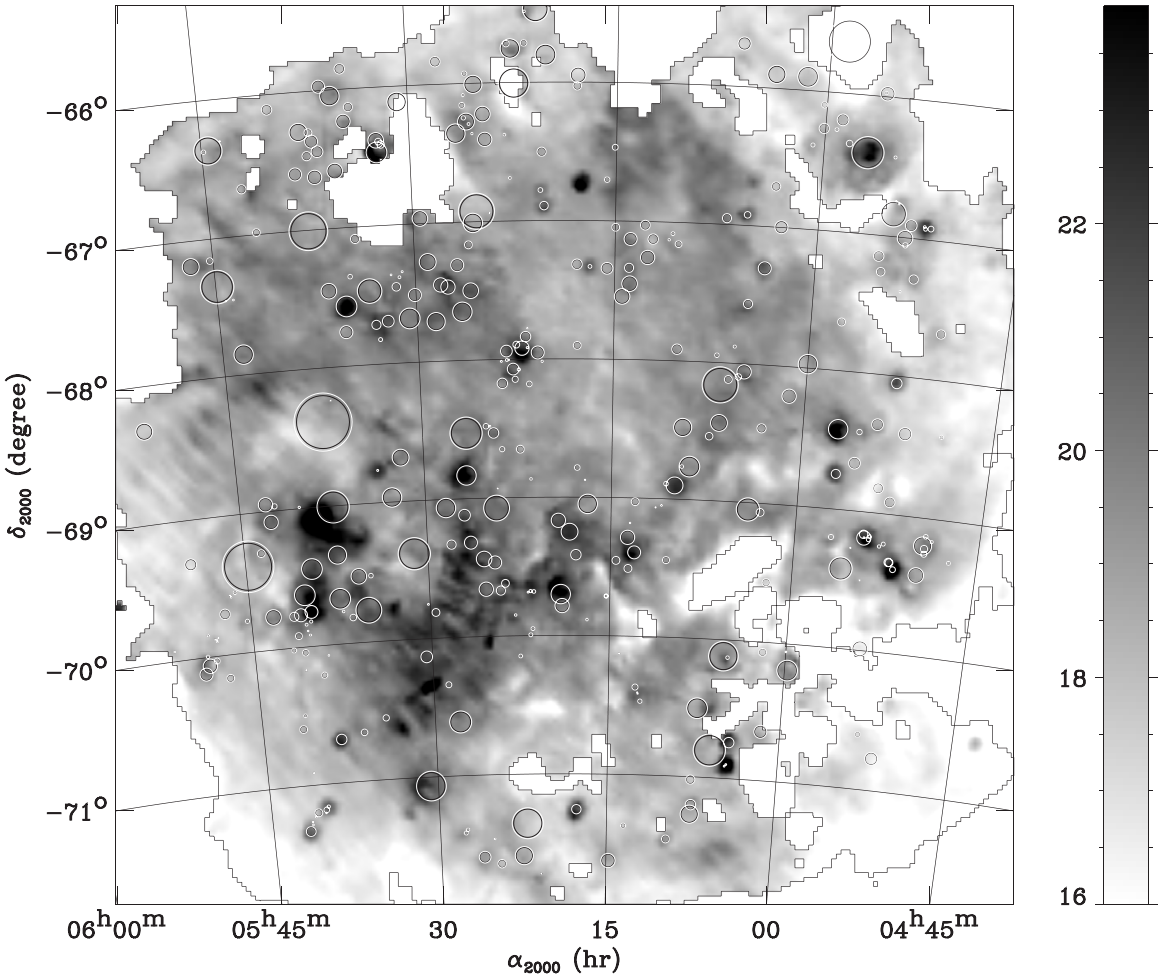

Figure 7. Map of the equilibrium temperature of the large dust grains, in K. Regions outside the contour drawn were removed based on their high-relative errors ($\Delta T/T > 0.3$). The overlaid symbols show the location and sizes of the H II regions in the catalog of Davies et al. (1976).

top-hat data or actual variations of the continuum shape. Note that, if our estimate actually underestimates the temperature, this will lead to overestimating the optical depth and the dust absolute abundance by a factor $\simeq$1.8, judging from the amplitude of the temperature difference for the whole LMC. Also note that this affects mainly the total dust abundance determination and not the other conclusions of this study, which are based on relative variations.

Local peaks of the temperature map show a good correspondence with the location of individual H II regions, indicating the presence of warm dust in those objects. No clear evidence is found in the map for the systematic presence of colder dust associated with MCs. This in principle could be due to the predominance of dust associated with neutral material along any line of sight. However, toward many GMCs in the LMC, the molecular column density is of the same order as the neutral one. The absence of a systematic trend for low temperatures toward regions detected in CO is therefore likely to indicate that in most cases, no large temperature difference exists between the dust associated with the neutral and the molecular gas. Note that detecting the presence of dust at very low temperature ($T < 10$ K) is not possible here and would require the use of sub-millimeter data.

Large-scale variations of the temperature are also seen. Most of the large-scale regions showing higher temperatures than the average can be understood as being heated by massive stars formed in the LMC, as discussed in Whitney et al. (2007, in preparation). One major exception to this picture is the large area near the center of the LMC, about 1° west of the molecular ridge (around $\alpha_{2000} = 5^{\rm h}30^{\rm m}$, $\delta_{2000} = -70°$) where the dust is found to be at $T_d \simeq 22$ K and no major site of massive star formation is known. This region corresponds to low total column density and emission (see Figure 1). However, the formal errors on the temperature at this location are of the order of 20% which rules out an artifact due to background subtraction errors. Also note that this region does not have a large 70 μm excess in Figure 6, indicating that unusually high contribution of VSG to the 100 μm brightness is not the reason for the warm temperatures observed. This warm region is well within the LMC stellar bar, although not at its center. Its shape does not match well the shape of the stellar bar nor does it correspond to the distribution of young stellar objects. Larger T_d values there could, in principle, be caused by the global heating of dust by the old stellar population. However, we note that the warm region is located just after the bright regions around 30 Dor, along the *IRAS* scan path, which mainly originates from the south ecliptic pole located just a few degrees north-east of the LMC. Residual stripes can be seen in the temperature map which point toward this direction and are due to the *IRAS* data at 100 μm. Although we use the IRIS product, which has been globally corrected for gain and offset variations, we cannot exclude that the warmer region could be the collective result of such uncorrected variations.

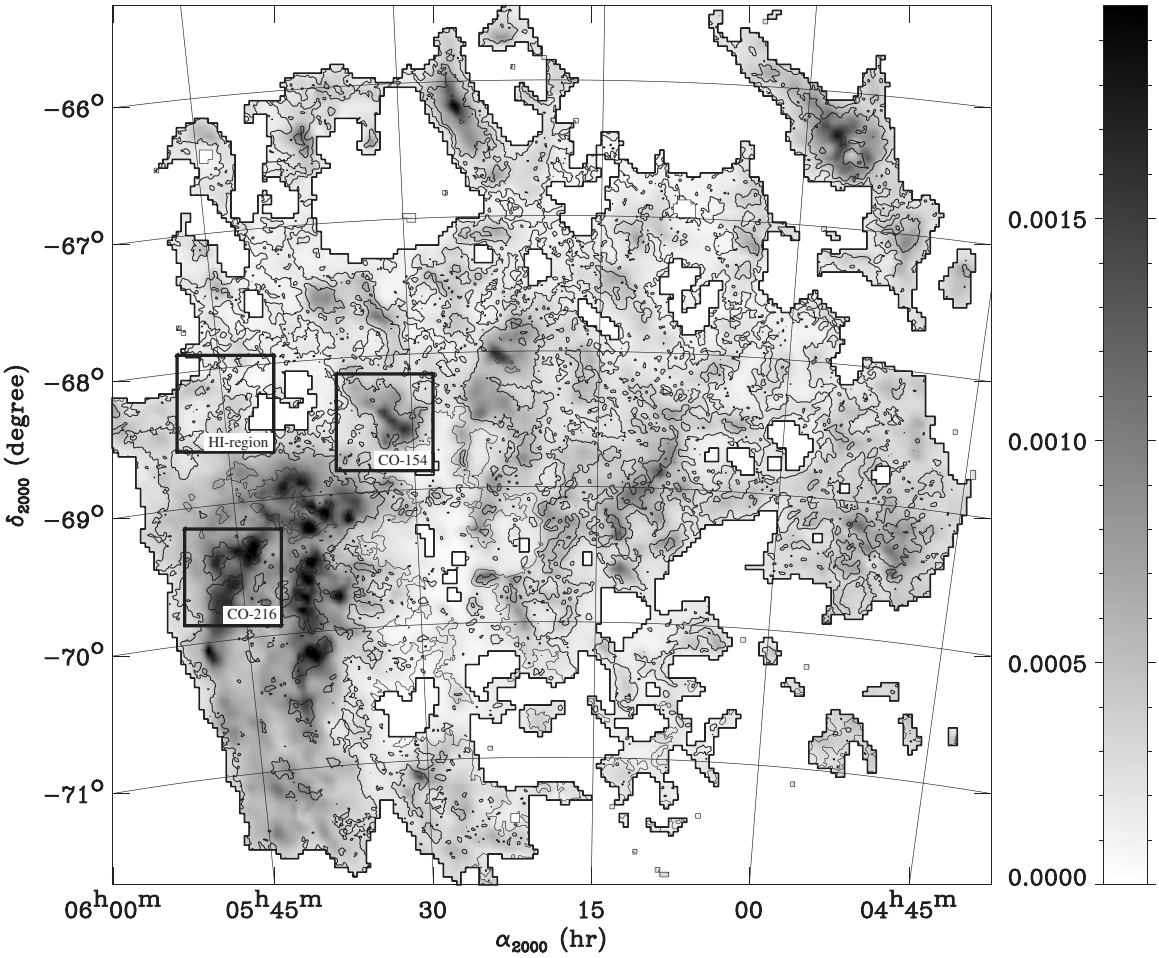

Figure 8. Map of the dust optical depth at 160 μm (see Section 6.2). White regions were removed based on their high relative errors. The contours show the distribution of the H I emission with the same contours as in Figure 1. The squares show the positions of the selected regions (see Figure 1).

6.2. FIR Excess Emission

Using the temperature map derived above, we construct a map of the dust optical depth at 160 μm, using

$$\tau_{160} = \frac{I_\nu^{160}}{B_\nu^{160}(T_d)}. \quad (9)$$

The optical depth map at 160 μm is shown in Figure 8. It is apparent that it shows a good overall spatial correlation with the column density as traced by H I and CO emissions. However, some significant departures from a linear correlation with these two tracers can be seen.

These departures can be evidenced in the map of $\tau_{160}/N_H^{\rm obs}$ shown in Figure 9 with $N_{\rm H}^{\rm obs} = \left(N_{\rm H}^{\rm H\,I,thin} + N_{\rm H}^{\rm CO}\right)$, where $N_{\rm H}^{\rm H\,I,thin}$ and $N_{\rm H}^{\rm CO}$ have been computed as stated in Sections 3.1 and 3.2, respectively. It can be seen that this quantity is maximum in a region located roughly at constant declination near $\delta = -69°30'$, as well as in an extended region just south of SGS11 and to the north of SGS11. As shown in the figure, these regions appear to correlate somewhat with H_α emission regions. However, the correlation remains poor and the excess could also originate from a different gas component other than the ionized medium. For instance, molecular gas with H_2 and no CO emission has been advocated to be responsible for a similar excess in the SMC (Leroy et al. 2007) and is often thought to be more abundant in low-metallicity galaxies (e.g., Madden et al. 1997), due to the higher overall radiation field intensity. An alternative explanation to the observed departures would be spatial variations of the dust abundance and/or emissivity properties.

If such an additional component is present, its column density $\left(N_{\rm H}^X\right)$ can be derived from the FIR emission assuming that it has a similar dust to total gas column density $\tau^{160}/N_{\rm H}$ than the H I and CO components. The corresponding gas column density can be deduced from the map of $\tau_{160}/N_{\rm H}^{\rm obs}$ using

$$\frac{N_{\rm H}^X}{N_{\rm H}^{\rm obs}} = \tau_{160}/N_{\rm H}^{\rm obs} \times (\tau^{160}/N_{\rm H})^{-1} - 1. \quad (10)$$

The emissivity value $\tau^{160}/N_{\rm H}$ can be derived from the lowest values in the map of $\tau_{160}/N_{\rm H}^{\rm obs}$, which correspond to regions where the additional component is assumed negligible. Taking the value at the lowest 5% level in the map of Figure 9 leads to $(\tau^{160}/N_{\rm H})_{\rm ref} = 8.8 \times 10^{-26}$ cm^2. Compared to the emissivity in the solar neighborhood

$$\left(\frac{\tau_{160}}{N_{\rm H}}\right)_{\rm SN} = \frac{\tau_{250}}{N_{\rm H}}\left(\frac{250}{160}\right)^2 = 2.44\times10^{-25}({\rm H\ cm^{-2}})^{-1}, \quad (11)$$

this corresponds to a dust abundance of 1/2.7. When compared to the MW disk abundance, this figure becomes 1/4.6, scaling with the total dust abundances derived for the MW plane and diffuse SED in Table 4. In the following, we consider the reference value $(\tau^{160}/{\rm N_H})_{\rm ref}$ as representative of the outer

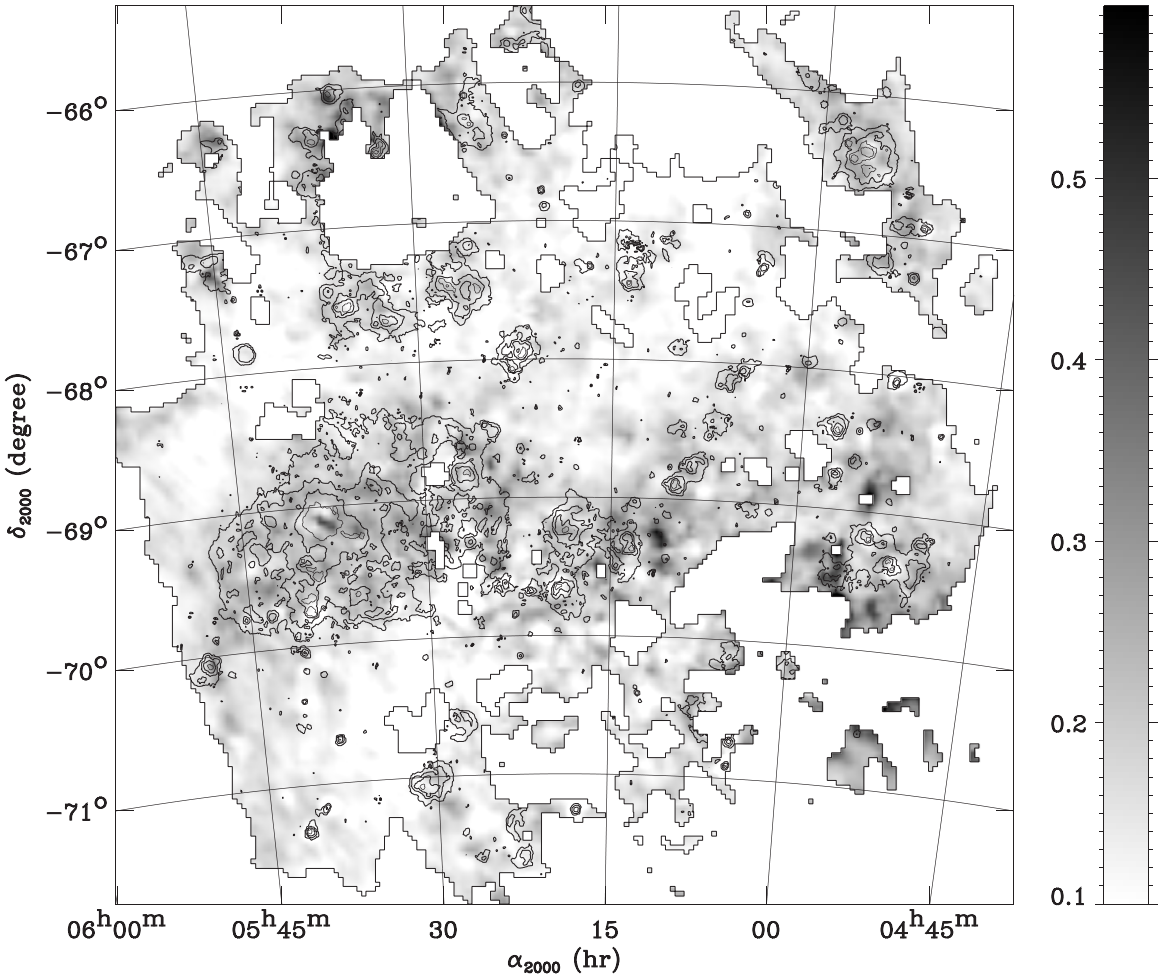

Figure 9. Map of $\tau_{160}/N_{\rm H}^{\rm obs}$ (see Section 6.2) in 10^{-4} for $N_{\rm H} = 10^{20}$ H cm^{-2}. White regions were removed based on their high relative errors. The contours show the distribution of the H_α emission with the same contours as in Figure 2.

regions of the LMC away from the additional gas component, and we call FIR excess emission any departure (which are mostly positive) from that value. The column density corresponding to the FIR excess is given in Figure 10. Note that only valid pixels are shown in the figure, where the combined relative error arising from the uncertainties on temperature and column densities is lower than 70%. The FIR excess is clearly correlated with the H I distribution. Integrating over the valid pixels of the map leads to a mass of $M^X = 3.3 \times 10^8 M_\odot$, about as large as the observed gas mass of H I and CO ($M^{\rm obs} = 3.0 \times 10^8 M_\odot$ as integrated over the same valid pixels), which itself is dominated by the H I component.

In order to understand the possible origin of the FIR excess, we performed the following linear correlation:

$$\tau_{160} = \tau_{NH}^{\rm H\,I} \times N_{\rm H}^{\rm H\,I} + \tau_{NH}^{\rm CO} \times N_{\rm H}^{\rm CO} + \tau_{NH}^{\rm H\,II} \times N_{\rm H}^{\rm H\,II} + cst, \quad (12)$$

where column densities are derived according to Section 3.

Since the H_α emission constrains only the emission measure, and not the column density of the ionized medium, we do not expect a linear correlation for this component, unless the density of the emitting medium can be considered constant along the line of sight. This approximation is probably valid only toward the most diffuse ionized gas, but invalid toward dense H II regions. Such approximation was used in the high-galactic-latitude ISM of the MW to identify dust emission associated with the diffuse ionized gas by Lagache et al. (2000).

Using Equation (12), we performed the correlation either in regions of the LMC with $I_{\rm H_\alpha}$ lower than some limit $H_\alpha^{\rm lim}$, therefore excluding from the data regions with bright H_α emission, or over the whole LMC (noted $H_\alpha^{\rm lim} = \infty$). The correlation results are given in Table 2.

It can be seen from Table 2 that τ_{160} is positively correlated with all three components (neutral, molecular, and ionized), indicating that dust FIR emission is well detected in all three gas phases. The correlation plots in Figure 11 are compared to the reference value obtained in the lowest brightness regions of the LMC ($(\tau^{160}/{\rm N_H})_{\rm ref} = 8.8 \times 10^{-26}$ cm^2). It can be seen that the correlation agrees with that slope at low $N_{\rm H}$ as expected, but becomes steeper at higher $N_{\rm H}$ values, indicating that the correlation is non-linear. Departure from the linear correlation is interpreted here as the existence of the FIR excess. Accordingly, the H I slopes derived when considering the whole LMC are steeper than in external regions with $I_{\rm H_\alpha} < H_\alpha^{\rm lim}$ because the FIR excess is strongest where the column density is higher, as already evident in Figure 10. For the same reason, the H I correlation coefficient is smaller when the fit is restricted to low H_α surface brightness regions. Disregarding the ionized component has little effect on the correlation factors for the H_I and CO components, showing that the H_α distribution is sufficiently decorrelated spatially from the two others and that its contribution, if not taken into account, remains in the residual map and is not attributed to one of the other components. This

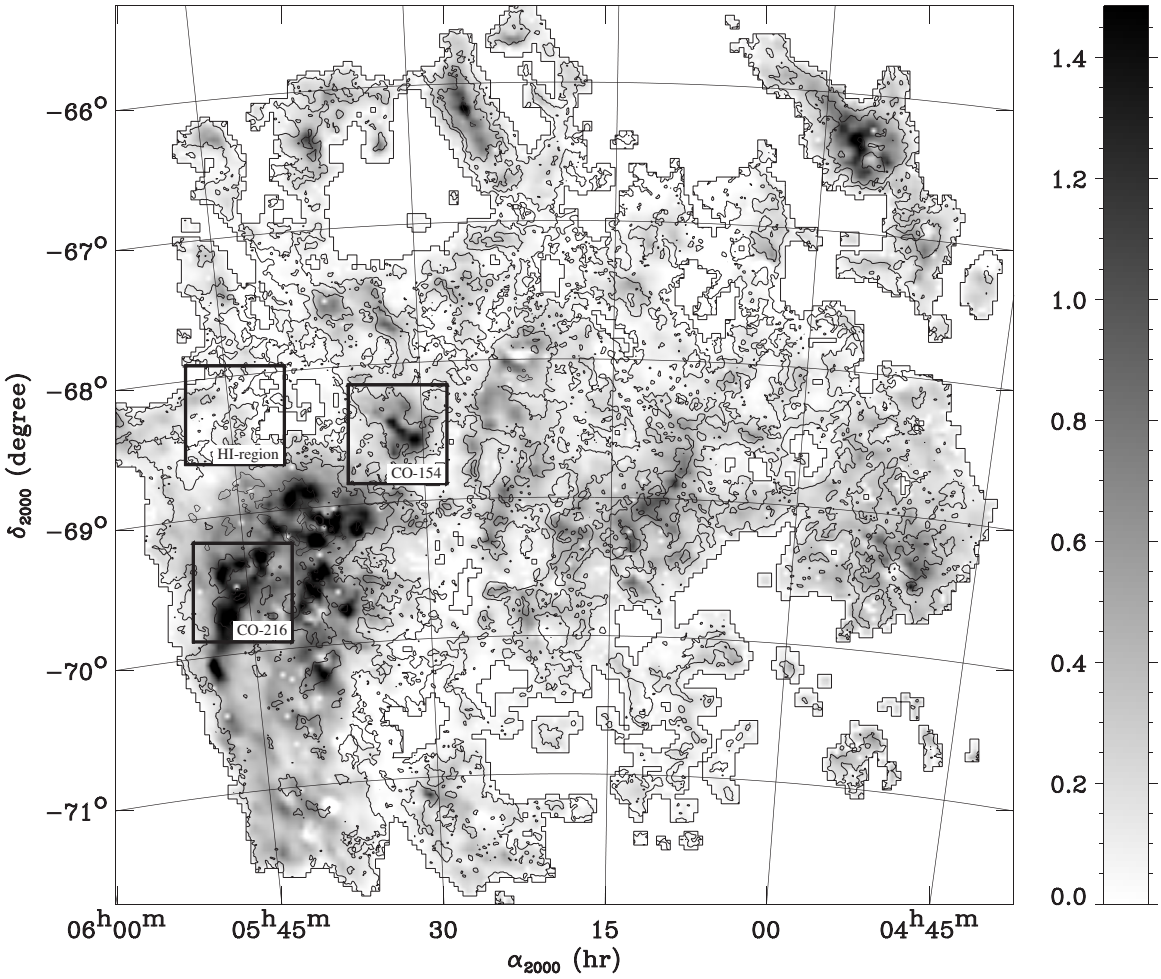

Figure 10. Map of $N_{\rm H}^{X}$ in units of 10^{22} H cm^{-2}. White regions were removed based on their high relative errors. The contours show the distribution of the H_I emission with the same contours as in Figure 1.

Table 2
Results of the Linear Correlation Between the Dust Optical Depth at 160 μm and the Observed Gas Components of the LMC

$H_\alpha^{\rm lim}$	$\tau_{NH}^{\rm H\,I}$	$\tau_{NH}^{\rm CO}$	$\tau_{NH}^{\rm H\,II}$	cst	$X_{\rm CO}$	n_e	χ^2/dof
Rayleigh	10^{-25} cm^2	10^{-25} cm^2	10^{-25} cm^2	10^{-5}	10^{20} H$_2$ cm^{-2} (K km s^{-1})$^{-1}$	cm^{-3}	–
∞	2.14 ± 0.03	0.67 ± 0.04	...	-7.06	2.18	...	3.55
20.00	1.47 ± 0.03	0.81 ± 0.04	...	-2.11	3.87	...	1.00
∞	1.98 ± 0.03	0.58 ± 0.03	0.12 ± 0.01	-5.58	2.05	1.67	3.23
20.00	1.48 ± 0.03	0.81 ± 0.03	1.97 ± 0.22	-3.36	3.81	0.08	0.63

Notes. The first two rows show the result of the linear correlation study, when excluding the ionized component from the fit. $H_\alpha^{\rm lim}$ (first column) is the H_α intensity threshold used to select pixels entering the correlation ($I_{H_\alpha} < H_\alpha^{\rm lim}$). $H_\alpha^{\rm lim} = \infty$ indicates no selection. Columns 2–5 give the best-fit parameters in Equation (12). The values of $\tau_{NH}^{\rm CO}$ and $\tau_{NH}^{\rm H\,II}$ are given for a reference $X_{\rm CO} = 7 \times 10^{20}$ H$_2$ cm^{-2} (K km s^{-1})$^{-1}$ and electron density of $n_e = 0.1$ cm^{-3}. Values of $X_{\rm CO}$ and n_e in Columns 6–7 correspond to the assumption of similar dust emissivity in the three gas phases through Equations (5) and (6) respectively. Errors are $3-\sigma$. The last column is the reduced χ^2 of the fit.

is true in both the cases where the correlation is carried over the whole LMC and where it is restricted to the faintest H_α emission. Using the $X_{\rm CO}$ value derived from the CO Virial analysis leads to $\tau_{NH}^{\rm CO} < \tau_{NH}^{\rm H\,I}$ by a factor 1.8. Alternatively, matching the two emissivities would require the conversion factor to be lower than the assumed value by the same factor leading to $X_{\rm CO} = 3.8 \times 10^{20}$ H$_2$ cm^{-2} (K km s^{-1})$^{-1}$. Similarly, the equality between $\tau_{\rm NH}^{\rm H\,I}$ and $\tau_{\rm NH}^{\rm H\,II}$ requires the density in the diffuse ionized medium given in Table 2 ($n_e = 8 \times 10^{-2}$ cm^{-3}), which is a reasonable value for the diffuse ionized ISM in comparison with values in the MW ($n_e \simeq 0.1$ cm^{-3}, e.g., Reynolds 2004).

Table 2 indicates that dust emissivity in the LMC is similar in the neutral and the diffuse ionized medium, as is the case in the MW (see Lagache et al. 2000). Given that the mass associated with the FIR excess is as large as that of the observed H I component, explaining the FIR excess by dust emission associated with the diffuse ionized emission would require $N_{\rm H}^{\rm H+} \simeq N_{\rm H}^{\rm H\,I}$. Such a large contribution from the ionized gas is unlikely under any realistic geometry of the diffuse gas. For instance, if we consider the area inside the first H_α contour in Figure 2 around 30 Dor (diameter $\simeq 1.4^\circ$), where the FIR excess is strong and significant H_α emission is observed, the typical H I

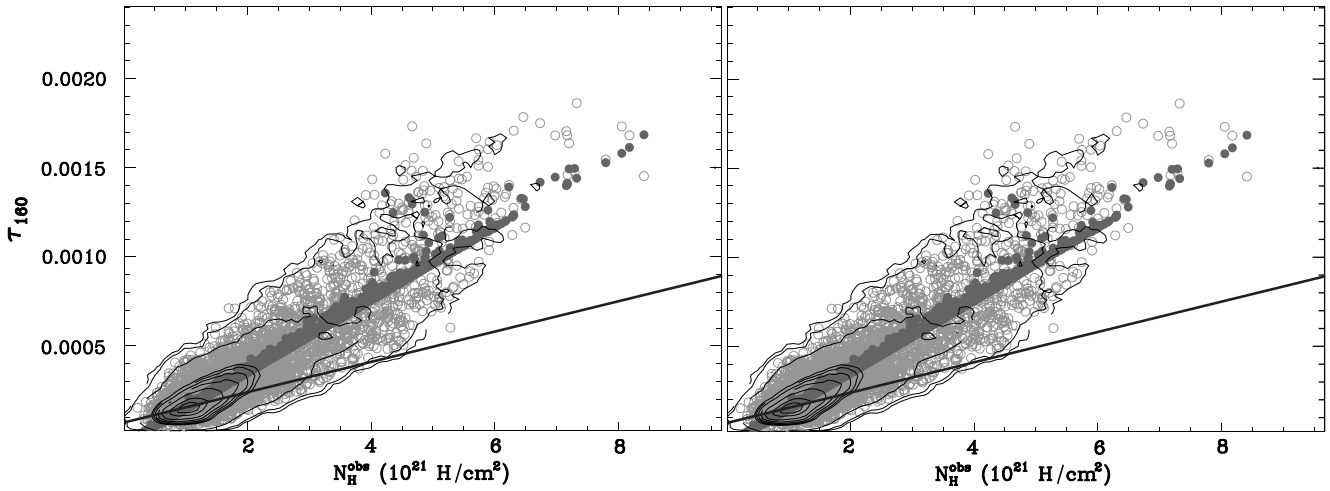

Figure 11. τ_{160} vs. $N_{\rm H}$ correlation. Left: over the whole LMC, right: in regions where $I_{\rm H_\alpha} < {\rm H}_\alpha^{\rm lim}$. The open symbols show the data and contours show the density of the open symbols. Filled symbols show the model, as given by Equation (12), for the best-fit parameters. On both plots, the straight line shows the correlation factor determined in low surface brightness regions of the LMC corresponding to $(\tau^{160}/N_{\rm H})_{\rm ref} = 8.8 \times 10^{-26}$ cm^2. The difference between this line and the observed correlation shows the importance of the FIR excess emission.

column density over this area is $N_{\rm H}^{\rm H\,I} \simeq 3.3 \times 10^{21}$ cm^{-2} and the typical H_α brightness over the same area is $I_{\rm H_\alpha} \simeq 120\,R$. Assuming that the extent of the ionized gas along the line of sight is the same as in the plane of the sky, we derive an average electron density of $n_e \simeq 0.4\,{\rm cm}^{-3}$. By using Equation (6), it translates into a column density for the ionized gas of $N_{\rm H}^{\rm H+} \simeq 3.5 \times 10^{20}\,{\rm cm}^{-2}$, which is lower than the required $N_{\rm H}^{\rm H\,I}$ by a factor of almost 10. A similar argument holds for other ionized regions of the LMC as well. Matching the two-column density values would therefore require an unlikely geometry where the corresponding ionized bubbles would have to be strongly elongated along the line of sight (LOS) (by a factor 100). We therefore conclude that the column density of the diffuse ionized gas in the LMC is too low to explain the observed FIR excess.

Similarly, we estimated the contribution from the C II line to the brightness in the *Spitzer* filter at 160 μm, by using the BICE (Balloon-Borne Carbon Explorer) map from Mochizuki et al. (1994) and smoothing 160 μm to the same angular resolution (14.9′). Across the LMC, the C II line contributes less than 10% of the 160 μm brightness, which also rules out this contribution as the origin of the FIR excess.

7. SELECTED REGIONS IN THE LMC

We selected several regions in the LMC for this study: one with no significant molecular emission in the NANTEN data (called H I − region in the following), and two regions containing molecular emission (called CO − 154 and CO − 216 following the denomination in the CO catalog of Fukui et al. 2008). The positions and general characteristics of these regions are given in Table 3. Clouds CO − 154 and CO − 216 are also referred to as CO-27 and CO37 respectively in the catalog resulting for the lower angular resolution survey of Cohen et al. (1988). The areas used for the IR/gas correlation around each target are shown in Figures 1–4. The selected regions are away from major H II regions and active star-formation regions, in order to avoid contamination of the SED by hot dust associated with those. The CO clouds CO − 154 and CO − 216 correspond to clouds 39 and 52 in the list of "large CO clouds" by Mizuno et al. (2001). Their CO luminosities are 3.8×10^4 K km s^{-1} pc^2 and 2.3×10^4 K km s^{-1} pc^2 respectively.

Table 3
Parameters for the Selected Regions in the LMC

Name	H I − region	CO − 154	CO − 216
α_{2000}	05:44:36	05:32:00	05:45:30
δ_{2000}	−68:16:12	−68:30:00	−69:33:00
Box size (°)	0.7 × 0.7	0.7 × 0.7	0.7 × 0.7
$T_{\rm H\,I}^{\rm a}$ (K)	18.5	19.9	18.7
$T_{\rm CO}^{\rm a}$ (K)	...	17.9	18.5
$N_{\rm H}^{\rm H\,Ib}$ (10^{20} H cm^{-2})	17.6	21.5	41.1
$N_{\rm H}^{\rm COc}$ (10^{20} H cm^{-2})	...	32.6	45.1
$X_{\rm CO}^{\rm d}$ H$_2$cm^{-2} (K km s^{-1})$^{-1}$	...	8.3	7.0

Notes.
[a] Computed using the I_{160}/I_{100} color ratio of the H I and CO correlated IR emissions, assuming $I_\nu \propto \nu^2 B_\nu(T_d)$.
[b] Mean H I column density in regions with $N_H^{\rm H\,I} > 1.2 \times 10^{21}$ H cm^{-2}.
[c] Mean CO column density in regions with $W_{\rm CO} > 1.2$ K km s^{-1}.
[d] Computed using the $L_{\rm CO}$-weighted average of the $X_{\rm CO}$ values derived from Virial analysis (Fukui et al. 2008) over the square region around each source considered in this paper.

7.1. SED of LMC Selected Regions

We calculate the SED of the selected regions in the LMC by correlating the emission at each IR *Spitzer* band with the H I and CO derived column densities, using

$$I_\nu = \left(\frac{I_\nu}{N_{\rm H}}\right)_{\rm H_I} N_{\rm H}^{\rm H\,I} + \left(\frac{I_\nu}{N_{\rm H}}\right)_{\rm CO} N_{\rm H}^{\rm CO} + I_\nu^{\rm res}, \qquad (13)$$

where $\left(\frac{I_\nu}{N_{\rm H}}\right)_{\rm H_I}$ and $\left(\frac{I_\nu}{N_{\rm H}}\right)_{\rm CO}$ are the dust emissivities in the neutral and molecular phases, respectively, and $I_\nu^{\rm res}$ is the residual emission. We do not include explicitly the H_α emission in the correlation, since H_α is not likely to be a linear tracer of the ionized column density. In the selected regions, the H_α emission is either very small (in the selected H I region) or exhibits a spatial distribution clearly independent of that of the H I and CO emissions (see Figures 1–3). The dust emission associated with this component is therefore likely to be accounted for in the residual term $\left(I_\nu^{\rm res}\right)$.

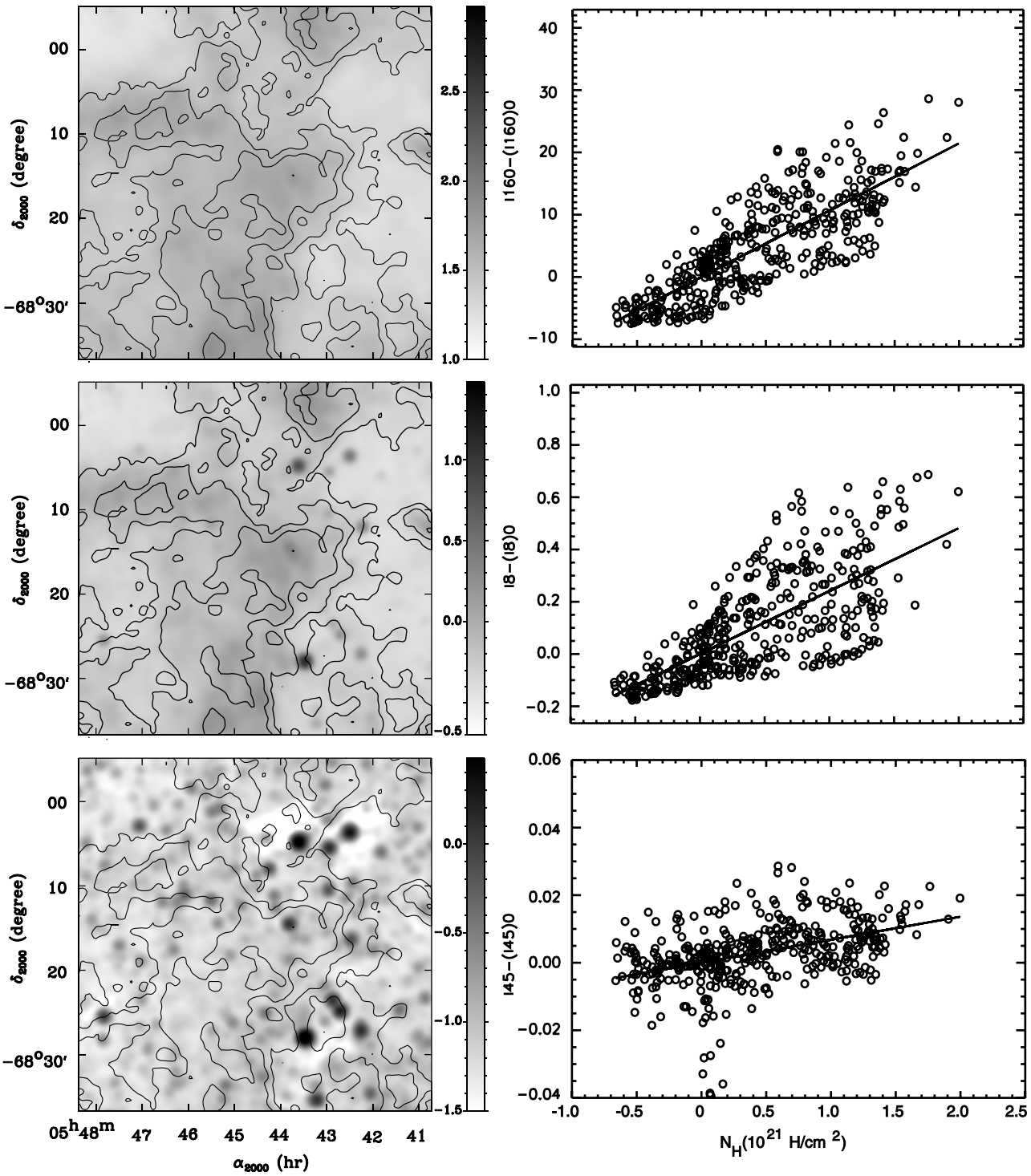

Figure 12. Left: SAGE images of the region H I − region at 160 μm (top), 8 μm (middle), and 4.5 μm (bottom). The gray scale is $\log_{10}(I_\nu(\mathrm{MJy\,sr^{-1}})^{-1})$. The region shown corresponds to the area used for the correlation. The contours show the H I integrated intensity levels at 1.2, 1.8, 2.4, and 3.6×10^{21} H cm^{-2}. The gray scale matches that of Figures 1, 3 and 4. Right: correlation plot for the corresponding wavelengths. The x-axis gives the total column density derived from the H I measurements. Data points at the resolution of 4′ are shown by the open symbols. The straight line shows the best model fit, corresponding to the coefficients in Table 5.

We combine *Spitzer* and IRIS data and therefore work at 4′ resolution, using the maps processed as described in Section 4. The slope of the IR/gas correlation is derived at each wavelength using a simple linear regression algorithm (the "regress" routine in IDL language) over the full spatial region, as shown in Figures 12 and 13. Examples of the correlation at several wavelengths are also shown in these figures. Error bars on the slope factor are derived using the statistical error on $H_H^{\mathrm{H\,I}}$, $W_{\mathrm{H}}^{\mathrm{CO}}$, and the IR data. In all cases, these errors were derived from the dispersion of the data in the background region (see Section 4).

The resulting correlation factors are given in Tables 5–7, and the corresponding SEDs are shown in Figures 14 and 16. It can be seen that the extended emission is detected at all wavelengths. The SEDs of selected regions were analyzed as explained in Section 8, and the results of the analysis are discussed in Section 9.

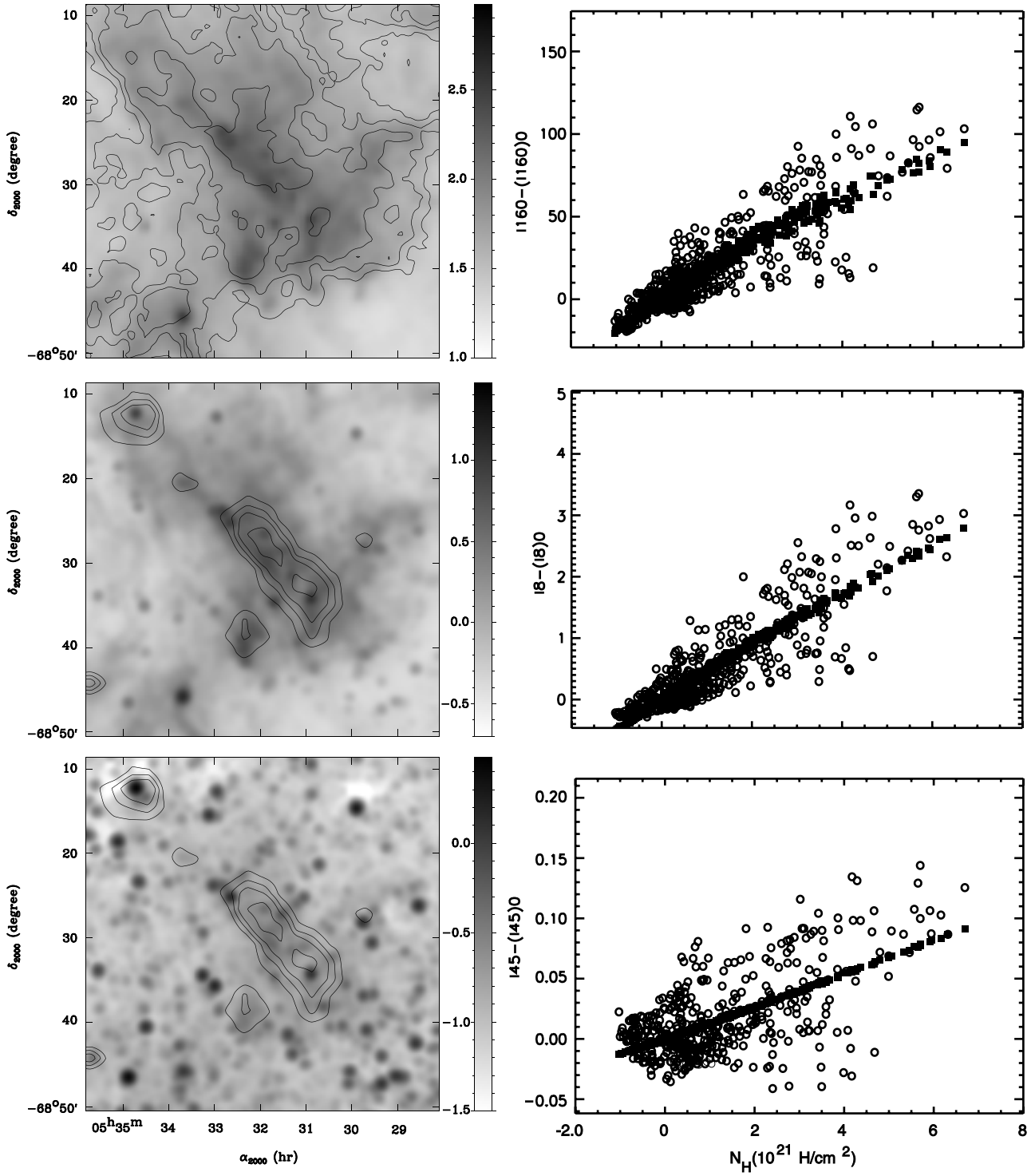

Figure 13. Left: SAGE images of the region CO − 154 at 160 μm (top), 8 μm (middle), and 4.5 μm (bottom). The gray scale is $\log_{10}(I_\nu(\mathrm{MJy\,sr^{-1}})^{-1})$. The region shown corresponds to the area used for the correlation. The contours on the top panel show the H I integrated intensity levels at 1.2, 1.8, 2.4, and 3.6×10^{21} H cm^{-2}. The contours on the middle panel show the CO integrated intensity levels at 1, 1.5, 2, and 3 K km s^{-1}. The gray scale matches that of Figures 1, 3 and 4. Right: correlation plot for the corresponding wavelengths. The x-axis gives the total column density derived from the H I and CO measurements. Data points at the resolution of 4′ are shown by the open symbols. The filled squares show the best model fit, corresponding to the coefficients in Table 5.

8. MODELING SEDs

We fit all SEDs analyzed in this paper using the model proposed by Désert et al. (1990), with the improvements described in Section 4.5.

We use a conjugate gradient method to adjust model parameters to the measured SEDs, while computing color corrections for the various instruments used. We choose to fit only the mass abundances of each dust species (Y_{PAH}, Y_{VSG}, Y_{BG}) as well as the intensity of the NIR continuum $\left(I_\nu^{\mathrm{NIR}}\right)$ and the ISRF strength (X_{ISRF}). We assume that the hardness of the ISRF is the same as in the solar neighborhood (i.e., we adopt the original ISRF from Désert et al. 1990), which we simply multiply by a single scaling factor X_{ISRF}. We refer to this model as run case 1. The results of the fit under this hypothesis are given in Table 4.

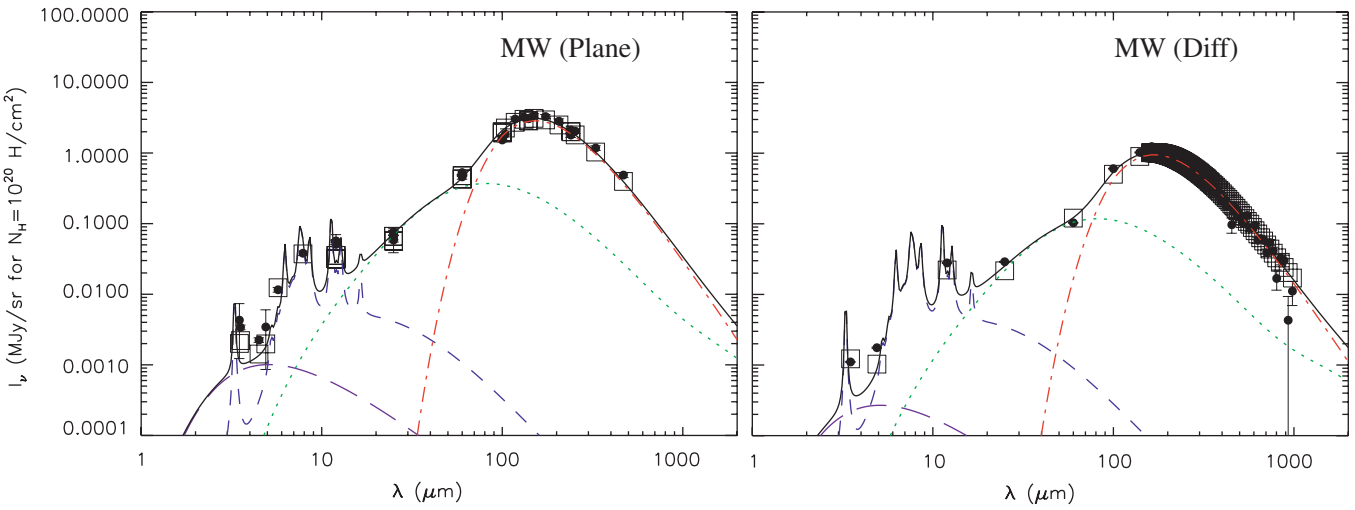

Figure 14. SED of the MW plane (left) and of the diffuse MW (right) (Dwek et al. 1997). The dots show the SED values and the squares show the corresponding prediction of the best model. The various curves show the model contribution from the NIR continuum (long dash), PAH (dash), VSG (dot), and BG (dot-dash) emission to the total spectrum (solid). All values are normalized to $N_H = 10^{20}$ H cm^{-2}. The model shown corresponds to case # 1 in Table 4.

(A color version of this figure is available in the online journal.)

Table 4
Results of the SED Fits

Region	Y_{PAH} (10^{-4})	Y_{VSG} (10^{-4})	Y_{BG} (10^{-3})	Y_{tot} (10^{-3})	NIR cont[a] (10^{-4} MJy/sr)	X_{ISRF} –	χ^2/dof –	Y_{PAH}/Y_{BG} (10^{-2})	Y_{VSG}/Y_{BG} (10^{-2})
MW (Désert)[b]	4.30	4.70	6.40	7.3	...	1.0	...	6.72	7.34
Run case 1									
MW (Plane)	3.11	10.9	8.42	9.82	10.1	1.46	7.87	3.69	13.0
MW (Diff)	4.83	6.38	4.68	5.80	2.69	0.80	11.87	10.3	13.6
LMC_All	0.97	3.47	3.16	3.60	24.72	1.85	1.12	3.07	10.97
H I – region (H I)	1.43	2.91	3.55	3.98	4.93	1.20	33.85	4.02	8.18
CO – 154 (H I)	1.83	4.39	4.05	4.67	6.69	2.47	12.46	4.51	10.84
CO – 216 (H I)	2.95	4.49	5.43	6.17	6.25	1.72	8.47	5.44	8.28
CO – 154 (CO)	0.80	2.47	0.98	1.31	15.24	3.55	7.09	8.17	25.18
CO – 216 (CO)	0.77	1.79	0.94	1.19	4.74	1.97	2.87	8.24	19.09
Run case 2 : $\alpha_{VSG} = 1.0$									
LMC_All	0.98	6.46	2.26	3.00	25.38	1.83	0.42	4.32	28.56
H I – region (H I)	1.58	5.62	3.29	4.01	3.63	1.19	14.49	4.80	17.07
CO – 154 (H I)	1.78	8.25	2.85	3.85	4.99	2.59	6.61	6.26	29.01
CO – 216 (H I)	2.69	6.01	4.51	5.38	6.86	1.91	4.74	5.96	13.33

Notes.
[a] Intensity of NIR continuum with $T_{eff} = 1000$ K at its I_ν peak for $N_H = 10^{20}$ H cm^{-2}.
[b] Original parameters from Désert et al. (1990).

In an attempt to quantify the 70 μm excess, we also allowed modification of the size distribution of the VSG. In the Désert et al. (1990) model, the number of VSG with size a is such that $n(a)da \propto a^{-\alpha_{VSG}}$ with $\alpha_{VSG} = 2.6$, explaining the data in the MW. We modified this value in order to obtain a flatter size distribution, therefore increasing the relative abundance of larger sizes. We found that $\alpha_{VSG} \simeq 1$ is necessary. We also show in Table 4 the best-fit results for models with $\alpha_{VSG} = 1$, referred to as run case 2.

The SEDs of the MWs and of selected atomic and molecular regions in the LMC are shown in Figures 14, 15, and 16, respectively. For those regions containing significant CO emission, the dust emission SEDs associated with both the neutral (H I) and the molecular (CO) emissions are presented. A reasonable fit is obtained in most cases. The most noticeable exceptions are for the LMC H I region, where the model overestimates the emission in the IRAC3 channel. This is reflected by the larger value of the reduced χ^2 for this SED in Table 4. It is also clearly visible that, unlike for galactic SEDs, the present model systematically underestimates brightnesses for the H I component of the LMC in the *IRAS* 60 μm and MIPS 70 μm channels, due to the presence of the 70 μm excess with respect to galactic colors, which was discussed in Section 5.3.

9. DISCUSSION

We discuss the implications of the observations, regarding the strength of the ISRF in the LMC, the relative abundance of the various dust species, including the possible origin of the 70 μm excess, as well as the absolute dust abundance. In all cases, we compare the results for the LMC with similar fits for the MW and solar neighborhood SEDs. Although SED fits in

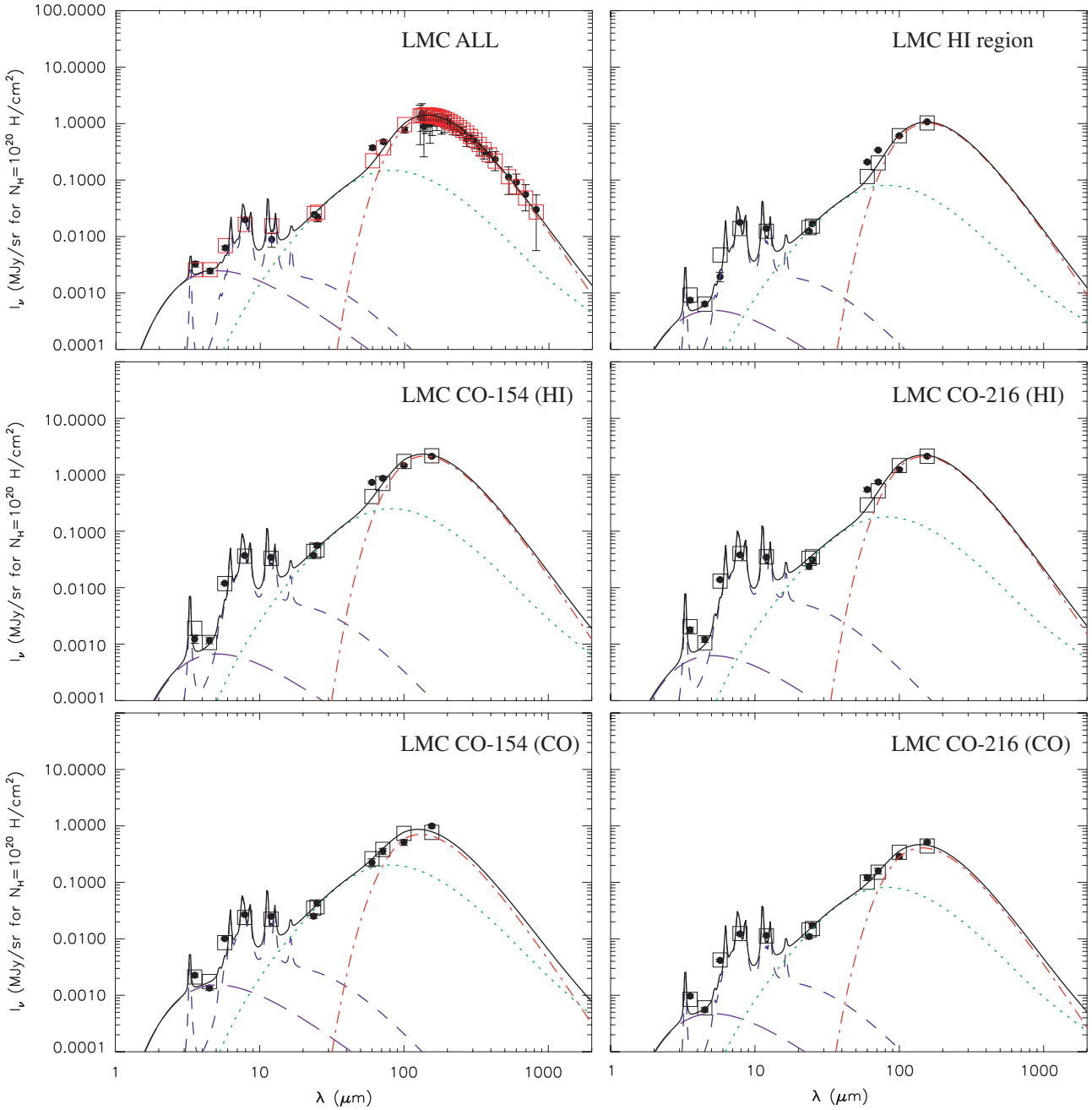

Figure 15. SEDs of selected regions in the LMC. Top left: SED of the total LMC, with stellar contribution subtracted. Top right: SED of the H I region (H I − region) selected in the LMC. Middle left: SED of the H I associated emission around cloud CO − 154. Middle right: SED of the H I associated emission around cloud CO − 216. Bottom left: SED of the CO associated emission around cloud CO − 154. Bottom right: SED of the CO associated emission around cloud CO − 216. Line styles and symbols have the same meaning as for Figure 14. All values are normalized to $N_{\rm H} = 10^{20}$ H cm^{-2}. The model fit shown corresponds to run case 1 in Table 4.

(A color version of this figure is available in the online journal.)

principle give information about absolute dust abundance, they are subject to the limitations imposed by the reliability of gas tracers. Therefore, the discussion about absolute dust abundance is mainly based on our global analysis presented in Section 6, while the discussion about relative dust abundances is mainly based upon the SED fit results.

9.1. ISRF Strength in the LMC

The ISRF strength values ($X_{\rm ISRF}$) vary from 0.8 for the diffuse galactic SED to 3.5 in one of the molecular regions selected in the LMC. Values of $X_{\rm ISRF}$ in the LMC are generally higher than in the solar neighborhood and galactic plane, with an average value of $X_{\rm ISRF} = 2.1$ for the average LMC emission. The elevated radiation field could be due to the existence of a higher stellar density and/or the existence of higher mass stars in the LMC. Note that in the MW, the IRSF intensity is known to vary significantly from the solar neighborhood value toward the inner molecular ring where it can reach about five times the local value, as evidenced in the results of galactic inversion of the IR emission (e.g., Paladini et al. 2007, and references therein). Similar variations are also likely to occur in the LMC. Similarly, it is likely that the spectral shape of the ISRF may vary across the LMC, due to the varying spectral type contributing most to dust heating, which might affect the dust abundances

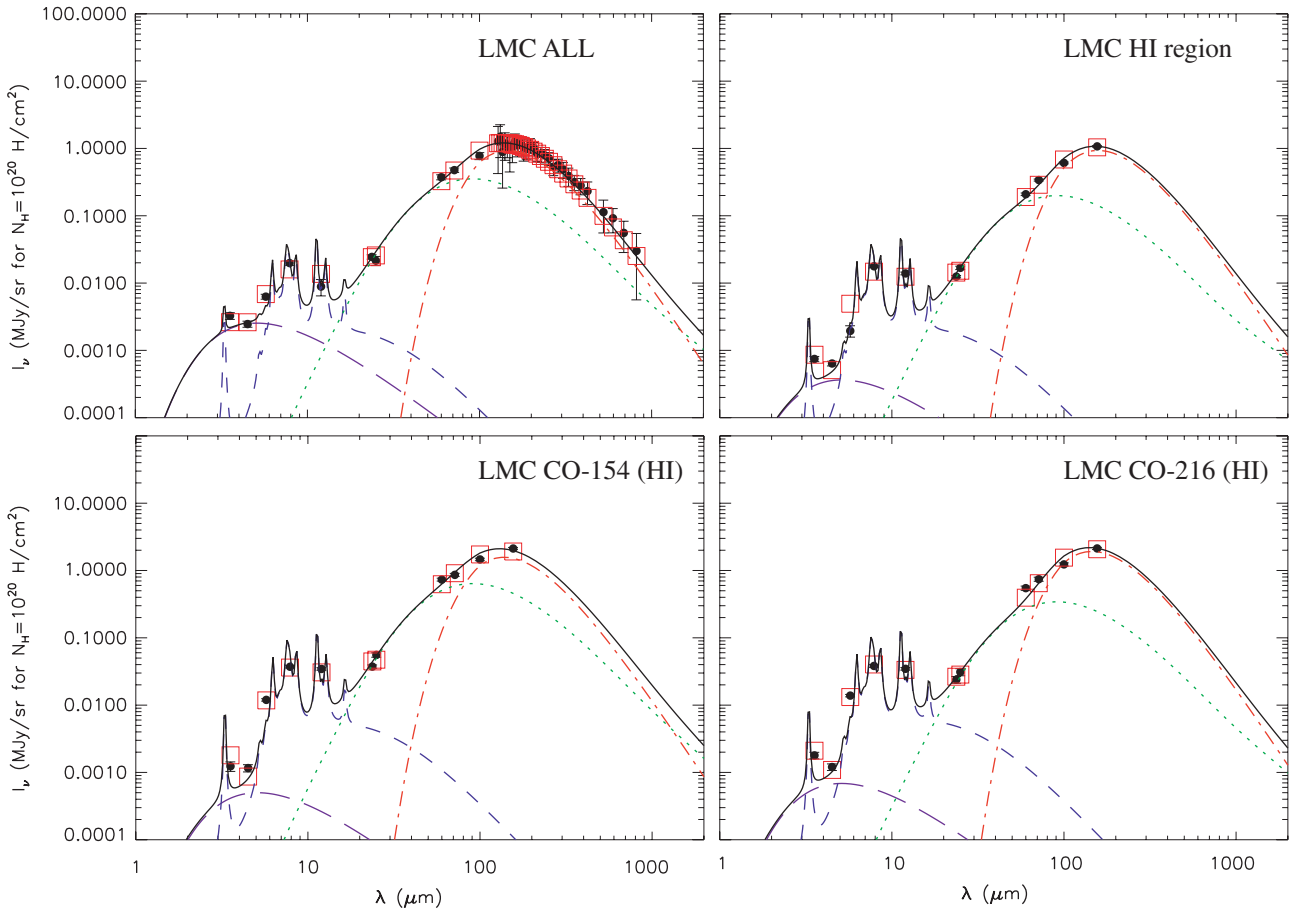

Figure 16. SEDs of selected regions in the LMC. Top left: SED of the total LMC, with stellar contribution subtracted. Top right: SED of the H I region (H I − region) selected in the LMC. Bottom left: SED of the H I associated emission around cloud CO − 154. Bottom right: SED of the H I associated emission around cloud CO − 216. Line styles and symbols have the same meaning as for Figure 14. All values are normalized to $N_{\rm H} = 10^{20}$ H cm^{-2}. The model fit shown corresponds to run case 2 in Table 4.

(A color version of this figure is available is the online journal.)

and composition derived. Note however that the moderate values and variations of $X_{\rm ISRF}$ measured here likely indicate only gentle variations of the spectral shape, unlike what is observed toward extreme low-Z galaxies such as those studied by Galliano et al. (2003).

9.2. Total Dust Abundance

Table 4 presents the abundance of dust correlated with atomic gas (traced by the H I 21 cm emission line) and molecular gas (traced by the ^{12}CO ($J = 1-0$) line emission). From SED fitting for atomic-correlated gas in the selected H I region, we measured a dust-to-gas mass ratio $Y_{\rm tot}^{\rm H\,I} = 4.0 \times 10^{-3}$. Similar fitting of the LMC SED as a whole yielded $Y_{\rm tot}^{\rm LMC} = 2.9 \times 10^{-3}$. Compared to the MW values for a region in the galactic plane and in the solar vicinity $\left(Y_{\rm tot}^{\rm MW} = 7.8 \times 10^{-3}, Y_{\rm tot}^{\rm SN} = 5.8 \times 10^{-3}\right)$, the dust-to-gas mass ratio therefore appears a factor of 2.7 lower in the LMC than in the MW plane. BG dominate the total dust mass, and are mainly responsible for the difference, but it can be seen that the VSG and PAH mass abundances follow the same MW/LMC trend, indicating that the effect is global. Note that depending on the assumptions made to account for the 70 μm excess, this figure could be slightly higher (e.g., $Y_{\rm tot}^{\rm MW}/Y_{\rm tot}^{\rm LMC} = 3.3$ in the run case 2 in Table 9.2). A similar $Y_{\rm tot}^{\rm MW}/Y_{\rm tot}^{\rm LMC}$ ratio of 4.6 was derived from the lowest $\tau^{160}/N_{\rm H}$ derived in Section 6.2, toward the faintest regions of the LMC. We therefore conclude that the average dust abundance in the LMC is $\simeq$3 times lower than in the MW but may vary spatially and be as low as $\simeq$4.6 times lower than MW in peripheral regions of the LMC. The low dust abundance values derived are consistent with the lower metallicity of the LMC. Further discussion about possible spatial variations of the dust abundance are given in Section 9.5.

9.3. Dust Composition

Let us use Table 4 to compare the relative abundance of the various dust components required to explain the SED for the diffuse emission in the MW (Dwek et al. 1997) (denoted MW (Diff)), the SED of the Galactic plane derived in Section 5.2 (denoted MW (Plane)), the star-subtracted, integrated LMC SED (denoted LMC_All), and the selected atomic and molecular regions of the LMC.

The last two columns of Table 4 show the mass ratio of PAH and VSG normalized to that of BG ($Y_{\rm PAH}/Y_{\rm BG}$ and $Y_{\rm VSG}/Y_{\rm BG}$ respectively). Note that such quantities are reasonably independent of the $X_{\rm ISRF}$ values, since both abundances vary in the same way with $X_{\rm ISRF}$ to first order. It can be seen from the values in Table 4 that the relative PAH abundance with respect to BG is about five times lower for the integrated LMC SED than in the solar neighborhood, and about 2.8 times lower than in the MW plane. The PAH abundance values in the selected LMC H I region, as well as in the neutral gas around the selected LMC molecular regions, are $Y_{\rm PAH}/Y_{\rm BG} \simeq 4.5 \times 10^{-2}$, which is only

about two times lower than the solar neighborhood value. This indicates either that the selected regions are not representative of the overall emission properties of the LMC in the neutral region or, more likely, that the total LMC SED is not dominated by the H I correlated component. We favor the second hypothesis. It is likely that the contribution associated with molecular material and diffuse ionized gas is much fainter than the H I contribution. Dust associated with H II regions could contribute a significant fraction of the total emission of the LMC. H II regions in our galaxy are clearly PAH deficient, as is shown by their low 12/100 *IRAS* ratios (e.g., Ryter et al. 1987), and the same seems to hold for H II regions in the LMC. Their dominance over the total emission could explain the apparent PAH deficit observed in the total LMC SED. Note that, for the MW SEDs, the influence of the H II regions probably explains the apparent difference (also by a factor of about 2) in PAH abundance between the galactic plane and the solar neighborhood values.

Inspection of Table 4 also indicates that the relative PAH abundance is higher toward molecular regions ($\simeq 8 \times 10^{-2}$) of the LMC than toward H I regions ($\simeq 4.5 \times 10^{-2}$). Although this would require confirmation on a larger set of molecular regions, this could be explained by the presence of PAH-rich halos similar to those which have been observed around translucent MCs in the MW (e.g., Bernard et al. 1993). In the solar neighborhood, such halos appear to have thicknesses of about 0.5 mag and PAH abundances enhanced by a factor of a few. At the distance of the LMC, the emission of such regions surrounding the MCs would appear correlated to the molecular material, at the resolution of the CO data used in the correlations. Higher-angular-resolution analysis relying on finer molecular data should allow us to test this hypothesis in the future.

According to Table 4, the relative abundance of VSG deduced from the total LMC SED is similar to that derived in the galactic plane ($Y_{\rm VSG}/Y_{\rm BG} \simeq 0.14$) and in the solar neighborhood, while the value derived for the selected H I region (and the H I correlated component surrounding the selected CO clouds in the LMC) is slightly lower ($Y_{\rm VSG}/Y_{\rm BG} \simeq 0.09$). The VSG abundance shows a trend similar to that of PAH, with a significant enhancement toward molecular regions ($Y_{\rm VSG} \simeq 0.21$) in comparison with the neutral regions ($Y_{\rm VSG} \simeq 0.09$). As for the PAH, this is in apparent contradiction with evidence in the MW that VSG are deficient in some molecular complexes (e.g., Abergel et al. 1994; Laureijs et al. 1991), but this could result from the contribution of halos located at the periphery of MCs and the limited angular resolution of the analysis here ($4'$ corresponding to 60 pc at the distance of the LMC).

Finally, we must note that the overall PAH and VSG abundances in the LMC are rather similar to MW values, unlike what has been observed toward extreme low-metallicity galaxies such as NGC 1569 by Galliano et al. (2003), which exhibit much higher radiation fields and very low PAH and VSG abundances. This clearly demonstrates that their exists very little commonality between the LMC and these types of galaxies.

9.4. *Possible Origin of the* 70 μm *Excess*

In Section 5.3 and Figure 6, we showed that the *Spitzer* color I_{70}/I_{24} has regional variations in the LMC. For the radiation field intensities representative of the LMC ($X_{\rm ISRF} \simeq 1$), the I_{70} brightness is contributed mainly by BG (60%) and VSG (40%), while the I_{24} brightness is contributed mainly by VSG (80%) and the "pseudocontinuum" of PAH (20%) according to the model used. Therefore, in principle, the observed variations could be due to abundance variations of any of the dust species. However, the SED fits of representative regions described in Section 8 clearly indicate that relative PAH abundances are very similar in all regions and to those in the MW, and cannot be taken to be responsible for the variations of the MIR spectrum. Similarly, variations of the BG abundance are smaller than would be required to explain the changes. BG temperature variations, through their impact on the Wien part of the BG emission, could influence the emission in the 70 μm band. These however were taken into account in the method used to derive the excess map. In addition, SED fits indicate that increasing the radiation field intensity does not allow us to explain the excess, when constraints at longer wavelengths (in particular 100 and 160 μm) are taken into account. In principle, the 70 μm excess could also arise from a significant contribution of the O I 63 μm (or O III 58 and 88 μm) line to the MIPS 70 μm band. However, such line contribution would have to be extremely bright to contribute significantly to the observed brightness at 70 μm. In addition, it should be accompanied by at least some C II 158 μm and O I 145 μm line emissions in the MIPS 160 μm band, which is not observed. Although shock fronts and high-density photodissociation regions (PDRs) (Kaufman et al. 1999) can generate relatively more 63 μm than 157 μm line emission, we consider line contribution an unlikely explanation for the excess. Note that this could be confirmed easily by spectroscopy measurements at locations selected from the 70 μm excess map, for instance with *Spitzer* itself or Herschel.

We therefore conclude that the most likely cause for the 70 μm excess is variations of the SED of VSG emission. In Section 8, we have shown that the 70 μm excess emission detected in the neutral phase toward the three selected regions of the LMC can be explained by modifying the VSG size distribution with respect to that of the MW, in a direction which corresponds to a flatter size distribution. This is equivalent to increasing the abundance of large VSG relative to smaller ones. Note that such a flattening of the size distribution was already invoked by Sakon et al. (2006) to explain the LMC IR emission. VSG coagulation may be expected to proceed in this fashion, though the geographic locations of the regions of 70 μm excess do not seem particularly conducive to grain coagulation. If VSG coagulation was responsible for the excess, we would also expect a decrease of the abundance of the smallest VSG with respect to MW values, which is not observed. In contrast, it seems that explaining the observed SED requires increasing the relative VSG abundance with respect to MW values by about a factor of 2. Shattering of larger grains in shocks could in principle produce such a mass increase of large VSG, which corresponds to about 13% of the BG mass. The fact that the 70 μm excess is observed exclusively toward the neutral medium and not in molecular regions would also favor such processes. However, grain shattering due to shocks should steepen the overall grain size distribution, increasing the abundance of VSG relative to big grains and also small VSG relative to larger VSG (Jones et al. 1996). Although the details of these processes are not sufficiently well understood to enable a detailed comparison to the observed effect, the size distribution change needed to explain the observations does not seem to match the predictions of dust shattering in shocks. In any case, the most likely interpretation remains that the increase of the abundance of larger size VSG is caused by erosion of even larger grains, since they are the most likely mass reservoir for the observed effect. Observational investigation using infrared spectroscopy and region-by-region color comparison of the

PAH, VSG, and BG may elucidate the cause of the 70 μm excess.

The 70 μm excess map and the SEDs of individual regions are compatible with the excess being mostly originating from the neutral or ionized phase. For instance, in the region around 30 Dor, the loop-like structure on the south-east has a similar spatial structure as the H_α emission, but the extension of the loop toward the south of 30 Dor shows no counterpart in the H_α emission and is only seen in the H I map. Inversely, there appear to be no correlation of the 70 μm excess with the molecular emission indicating that the excess is smaller and probably consistent with zero in MCs. The selected cloud CO − 154 is one of the rare occurrences where a positive correlation is seen in Figure 6, but analysis of the SED of this cloud indicates that this may be an artifact of the temperature determination based on the 160/100 ratio. Note that a significant decrease of the *IRAS* I_{60}/I_{100} *IRAS* color has been evidenced in some MCs in the solar neighborhood (e.g., Abergel et al. 1994; Laureijs et al. 1991). Interestingly, the lack of 70 μm excess observed here in the LMC could have the same origin. Since the material in MCs is relatively more shielded from the interstellar radiation field, we would expect dust there to be colder; the higher densities and lower temperatures may also allow some grain coagulation. The total abundances of VSG and BG toward the LMC MCs are comparable to or even larger than in the diffuse medium. If the lower 70 μm excess in MCs was due to VSG properties, then the observations require that the total mass of VSG remains high, but there are relatively more of the small VSG. It is unclear why the MCs would have a steeper size distribution of VSG while retaining a high VSG mass. If the largest VSG were to coagulate onto the big grains, then the size distribution would steepen but the mass would decrease. It might have been expected that the smaller VSG would coagulate first, owing to their higher surface area per unit mass, but the details of grain coagulation are insufficiently understood to relate the observed effect to theoretical predictions.

9.5. Possible Origin of the FIR Excess

The IR measurements provide a reasonably reliable measure of the dust column density for a given line of sight, as long as the dust has a roughly constant temperature along the line of sight, or the temperature dependence can be removed. The map of the dust optical depth at 160 μm constructed in Section 6.2 should therefore trace the total ISM column density. The FIR excess was evidenced in Section 6.2 as a departure from the linear correlation between the FIR dust optical depth τ^{160} and the observed column density (see Figure 11). Outer regions of the LMC with lower total column density have lower emissivity than inner regions. In principle, this can be explained either by spatial variations of the dust abundance or by the existence of an additional gas component, undetected with the available tracers and leading to underestimation of the total gas column density. As discussed earlier, such an additional phase would have to be correlated mainly to H I (see Figure 10) and its mass should be about twice the optically-thin H I mass in order to account for the observations, if dust abundance is assume constant. The additional phase could be either due to optical depth effects in the H I measurements or due to the presence of a pure H_2 phase where CO is not present or not excited.

9.5.1. Dust Abundance Variations

If dust abundance variations are invoked to explain the FIR excess, and it is assumed that no FIR excess exists in the regions of the LMC with the lowest apparent τ^{160}/N_H, the total dust abundance would have to increase by a factor of $\simeq$2 from the outer regions of the LMC, where $Y_{tot}^{MW}/Y_{tot}^{LMC} = 4.6$ (see Section 9.2) to the inner regions where we would then expect $Y_{tot}^{MW}/Y_{tot}^{LMC} = 2.3$. The distribution of the excess FIR emission (see Figure 10) clearly shows stronger values where most star formation takes place, which could reflect the production of dust by present and past star formation. Accordingly, it can be seen from Table 4 that the total dust abundance needed in the H I phase surrounding the three regions we selected increases from the H I region, which is located in a low FIR excess area of Figure 10, to the CO − 216 cloud, which is located in a bright FIR excess region.

Table 4 shows that, if dust abundance variations are allowed, the dust abundance derived in the molecular phase of the two selected MCs in the LMC is lower than that derived for the neutral phase surrounding them by a factor of about 3.7. This variation is caused mainly by BG which dominate the total dust mass, but is also reflected by the VSG and PAH abundances. No astrophysical model exists that could explain a lower abundance of the large dust grains in MCs relative to the surrounding neutral medium, and similar variations have never been reported in the MW. It is therefore likely that this reflects either a change in the optical properties of the dust or a problem with the determination of the gas column density as derived from CO measurements.

In the solar neighborhood, an increase of the grain emissivity by a factor of 3–4 has been advocated to explain the abnormally low temperature observed in some translucent MCs (Bernard et al. 1999; Stepnik et al. 2003). This is interpreted as resulting from the formation of fractal dust aggregates, which is usually accompanied by a steep decrease of the VSG emissivity, understood as mutual aggregation of the two species. Therefore, dust aggregation is expected to increase the dust emissivity, while the variation observed here in the LMC is of a *decrease* of the emission in the molecular regions; furthermore, we do not observe a simultaneous decrease of the total VSG abundance in the molecular phase, as observed in some cold MCs in the MW where coagulation is suspected to happen. It is therefore unlikely that changes in the optical properties of the dust can explain the effect.

Rather than the dust emissivity being depressed in the molecular gas, it could be that the gas column density has been overestimated. We used the CO line, assumed to arise from Virialized clouds, to estimate the gas column density. Assuming that, in the absence of intrinsic optical property variations, the total dust abundance is the same in the H I and CO phases of each selected MC, then we can solve for $X_{CO} = 2.5 \times 10^{20} f_{H\,I}\,H_2\,cm^{-2}\,(K\,km\,s^{-1})^{-1}$ and $X_{CO} = 1.7 \times 10^{20} f_{H\,I}\,H_2\,cm^{-2}\,(K\,km\,s^{-1})^{-1}$ for clouds CO − 154 and CO − 216 respectively. These values are in the range of accepted values for the inner galactic disk: 1–3 $\times 10^{20}\,H_2\,cm^{-2}\,(K\,km\,s^{-1})^{-1}$ (Bloemen et al. 1986; Solomon et al. 1987) if $f_{H\,I} \sim 1$. However, the galactic value is significantly lower than the average value for the LMC derived from the Virial analysis of the first NANTEN LMC survey, $X_{CO} = 9 \times 10^{20}\,H_2\,cm^{-2}\,(K\,km\,s^{-1})^{-1}$Mizuno et al. (2001). A more careful comparison on a cloud-by-cloud basis is not straightforward, since the analysis presented here involves a correlation around a region of the sky which generally includes several CO clumps. Averaging the latest Virial X_{CO} values by Fukui et al. (2008) weighted by the CO luminosity of the clouds over the correlation region leads to average Virial values of $8.3 \times 10^{20}\,H_2\,cm^{-2}\,(K\,km\,s^{-1})^{-1}$ and $7.0 \times 10^{20}\,H_2\,cm^{-2}\,(K\,km\,s^{-1})^{-1}$ for clouds

CO − 154 and CO − 216 respectively. Therefore, the Virial analysis leads to X_{CO} values higher than those derived from the infrared-H I-CO analysis by a factor of $\sim 3.7/f_{HI}$. Inaccurate estimate of the X_{CO} factor from the Virial analysis, due to the limited angular resolution of the NANTEN data, could be responsible for the observed discrepancy. However, recent estimates of the X_{CO} factor based on higher resolution data using the MOPRA telescope (A. Hughes 2007, private communication) lead to results similar to those derived by Fukui et al. (2008). We therefore consider it unlikely that X_{CO} values derived from the Virial analysis could be overestimated by such a large factor. This leads to the conclusion that dust abundance variations are unlikely to be responsible for the FIR excess.

9.5.2. Additional Gas Component

The alternative explanation of an additional gas phase, correlated to the H I distribution, could explain the FIR excess. If such a component were strongly correlated with the H I component in the LMC at the scale we have performed the analysis, it would result in underestimating the actual column density and therefore overestimating the corresponding emissivity toward the H I phase in our analysis, independent of the origin of the additional gas phase. It would also naturally explain a difference in X_{CO} of a factor of 3, when the additional components, not taken into account in the correlations (see Equation (13)), double the H I column density.

The existence of an additional gas phase with no apparent CO or H I emission has already been evidenced in our own Galaxy through correlation of either the IR and extinction data (e.g., Meyerdierks & Heithausen 1996) or the gamma-ray and IR emission (Grenier et al. 2005). In the MW, the inferred mass of the dark phase is similar to that of the molecular gas traced by CO emission (Grenier et al. 2005), which presumably corresponds to a total mass close to that of H I over the same area, a situation similar to what we observe here in the LMC. In the case of the LMC, we propose that the additional component could be due to the presence of either cold H I or a pure H_2 phase or a combination of both. Analysis of the full IR emission distribution of the LMC could help clarify this issue, as well as complementary approaches using extinction or gamma-ray emission.

Cold H I. The 21 cm line measures the atomic gas column density if we assume the gas to be optically thin or if we know the excitation temperature of all the gas. Recall that at column densities $>10^{21}$ cm^{-2} and for gas with spin temperature $T_s = 60$ K, the column density can be three times higher than would be inferred if the line is assumed to be optically thin. If the emissivity in the H I-emitting medium is in error by a factor f_{HI} due to underestimation of the H I column density, then (1) the dust-to-gas ratio in the diffuse atomic medium decreases by f_{HI} and (2) the value of X_{CO} derived assuming the same emissivity for atomic and molecular gas increases by f_{HI}. If $f_{HI} \simeq 3$, which is plausible as discussed in Section 3.1, then X_{CO} inferred from the infrared analysis matches that inferred from the line-width and size analysis of the CO data. Note that, in that case, the total mass of the molecular phase as traced by CO in the LMC is very small, only 1/30th of the total gas mass.

Pure H_2 phase. The CO emission measurements provide the molecular gas column density if the CO emission arises from Virialized clouds. But if there is significant H_2 in regions without CO or where the CO is faint, then we would detect "excess" FIR emission with respect to the gas column density estimated from the 21 cm and CO images. This component could correspond to a phase where H_2 molecules are formed, but CO is still preferentially photodissociated, as as been proposed to explain the emission properties of other low-metallicity systems such as 30 Dor (Poglitsch et al. 1995), the SMC (Leroy et al. 2007), or more distant low-metallicity galaxies such as IC10 (Madden et al. 1997).

For the high-galactic-latitude sky in the MW, it was found that "infrared excess" (with respect to H I column density) is closely associated with MCs where CO had been observed (Reach et al. 1998). Follow-up observations detected 47% of northern infrared excess clouds; indeed 72% of infrared excess clouds with dust temperature below average were detected in CO (Onishi et al. 2001). We expect that locations with FIR excess and low dust temperature would also be associated with molecular gas in the LMC. However, at the 4′ resolution of the analysis carried here, even the known CO clouds fail to show significant temperature decrease, possibly due to warm cloud halos. Thus while some of the FIR excess is likely to arise from H_2 clouds without CO, the actual H_2 content is difficult to assess. In particular, it is unclear if the mild increase of the ISRF strength in the LMC, combined with the observed lower total dust abundance, could explain the predominance of this phase.

9.5.3. Consequence for Dust Abundance

Understanding the limitations of the H I, infrared, and CO data, we can now interpret the dust-to-gas ratio. For the atomic gas, we measure a dust-to-gas mass ratio that is approximately $2.1/f_{HI}$ times lower than that found in the MW. The metallicity of the LMC inferred from stellar atmospheres and H II regions is lower than the solar vicinity by a factor of 2.0, averaging over all elements; for the important and well-measured dust-bearing elements C, O, and Fe, the LMC abundance is lower than solar vicinity by factors 1.9 ± 1.0, 2.2 ± 0.4, and 1.5 ± 0.8, respectively (Russell & Dopita 1992). We expect that the dust-to-gas ratio in the LMC would be lower than that in the MW by *at least* as much as the metals out of which they are combined; this condition appears to be satisfied for any valid f_{Hi}. From a comparison of extinction and Lyα absorption, the dust-to-gas was found to be lower than that in the MW by a factor 3.3 ± 0.9 (Kornreef 1982), and 3.7 ± 0.4 for the LMC2 supershell and 1.7 ± 0.15 for average LMC samples (Gordon et al. 2003). The ultraviolet results and our infrared result are compatible for $f_{HI} \sim 1$ (relative to the LMC average sample) or $f_{HI} \sim 1.8$ relative to the LMC2 sample; such values of f_{HI} are plausible as discussed above.

10. CONCLUSIONS

We presented a global analysis of the FIR emission in the LMC, based on the combined analysis of the *Spitzer* SAGE data and ancillary data tracing the gas emission. We determined the SED in three individual regions of the LMC selected to show little star-formation activity and be located away from major H II regions. We showed that extended emission of the neutral, molecular, and diffuse ionized phase is detected at all IR wavelengths from 3 μm to 160 μm. Modeling of the SEDs of these regions shows that the relative abundance of the various dust species is similar to that in our own MW. The integrated SED of the LMC shows lower relative PAH abundance than individual regions, which can probably be explained by the contribution from H II regions. PAH and VSG abundances appear slightly higher in the molecular than in the neutral phases in the selected regions, which we interpret as

enhanced abundance of small dust particles in unresolved halos surrounding MCs.

We showed that a significant emission excess is present at 70 μm with respect to expectation for VSG and large grain emission based on the 24 μm and 160 μm emissions respectively. The 70 μm excess increases gradually from the MW to the LMC to the SMC, suggesting an increase of the excess with decreasing metallicity. The excess is essentially associated with the neutral medium, and is not present in the molecular phase. The strongest excess region is a loop around a position just south of 30 Dor. We show that it is possible to explain the 70 μm excess by a modification of the size distribution of VSG with respect to MW standards and an associated VSG mass increase corresponding to 13% of the total dust mass. We propose that the 70 μm excess could be due to the production of large VSG through erosion of larger grains in the diffuse medium.

We constructed all-LMC maps of the temperature and FIR optical depth of large dust grains at a resolution of 4′, by combining the *Spitzer* 160 μm and *IRAS* 100 μm images. The temperature map shows variations in the range $12.1 < T_d < 34.7$ K and a systematic gradient from inner to outer regions tracing the general distribution of massive stars and individual H II regions. Departures from this are also identified, in particular we evidenced a warm extended region, within the stellar bar, which may indicate the presence of dust heated by the old stellar population. No systematic decrease of the temperature was evidenced toward MCs.

Using the temperature map derived from the FIR emission, we constructed a map of the dust optical depth at 160 μm. Although the optical depth correlates globally with the H I gas distribution, a clear departure from a linear correlation exists. Using the measured emissivity value toward low column density as a reference, it leads to a FIR excess at high $N_{\rm H}$. Several possible interpretations of the FIR excess emission were investigated, in particular the presence of an additional gas component undetected in the available gas tracers and intrinsic variations of the dust/gas ratio or dust optical properties. We show that, under the assumption of constant dust abundance and emission properties in all ISM phases, additional gas would have to be as massive as the presently-known, optically-thin gas in the LMC. We showed that it is plausible that the FIR excess is due to cold gas that is optically thick in the 21 cm line. Other possibilities include a pure H_2 phase with no CO emission or a "dark phase" similar to that evidenced in the MW by gamma-ray studies.

A systematic increase of the dust abundance with increasing gas column density could also be responsible for the non-linear correlation observed. Under this hypothesis, the dust abundance would increase by a factor of 2 from the most diffuse regions at the periphery of the LMC to the densest regions where stars are formed. We note, however, that under this hypothesis, values of the CO-to-H_2 conversion factor ($X_{\rm CO}$) are uncomfortably low (by a factor of 2) with respect to those derived from the Virial analysis of the CO data.

On the one hand, if an additional gas component is invoked, dust abundance in the LMC is estimated to be about 4.6 times lower than in the MW. On the other hand, if variations of the dust abundance are invoked to explain the FIR excess, dust abundance would vary from 4.6 to 2.3 times lower than MW from the outer to the inner regions of the LMC. A firm conclusion regarding the origin of the FIR excess will have to await future and more detailed studies of the SAGE data.

We are grateful for E. Dwek who provided the MW SED of the diffuse emission at high galactic latitudes.

APPENDIX

SED TABLES

Tables 5, 6, and 7 contain the SEDs for the various components studied.

Table 5
Spitzer SED of the Various Components Studied Here

Name	IRAC1	IRAC2	IRAC3	IRAC4	MIPS1	MIPS2	MIPS3
MW (Plane)	3.40×10^{-3}	2.25×10^{-3}	1.16×10^{-2}	3.81×10^{-2}	...	...	...
MW (Plane)(Err)	3.42×10^{-4}	2.23×10^{-4}	1.16×10^{-3}	3.81×10^{-3}	...	...	...
MW (Diff)	...	...	...	...	...	...	...
MW (Diff)(Err)	...	...	...	...	...	...	...
LMC_All	1.39×10^{-4}	1.31×10^{-4}	3.02×10^{-3}	1.76×10^{-2}	2.81×10^{-2}	4.95×10^{-1}	1.11
LMC_All(Err)(Err)	1.18×10^{-3}	8.30×10^{-4}	7.50×10^{-4}	2.04×10^{-3}	3.07×10^{-3}	5.25×10^{-2}	1.18×10^{-1}
H I − region (H I)	7.46×10^{-4}	6.38×10^{-4}	1.95×10^{-3}	1.78×10^{-2}	1.25×10^{-2}	3.39×10^{-1}	1.07
H I − region (H I)(Err)	8.78×10^{-5}	6.75×10^{-5}	4.99×10^{-4}	8.81×10^{-4}	6.55×10^{-4}	1.57×10^{-2}	3.91×10^{-2}
CO − 154 (H I)	1.23×10^{-3}	1.16×10^{-3}	1.20×10^{-2}	3.71×10^{-2}	3.74×10^{-2}	8.62×10^{-1}	2.12
CO − 154 (H I)(Err)	2.65×10^{-4}	1.92×10^{-4}	6.71×10^{-4}	2.03×10^{-3}	2.94×10^{-3}	5.96×10^{-2}	1.02×10^{-1}
CO − 216 (H I)	1.79×10^{-3}	1.20×10^{-3}	1.38×10^{-2}	3.82×10^{-2}	2.39×10^{-2}	7.43×10^{-1}	2.13
CO − 216 (H I)(Err)	2.65×10^{-4}	1.81×10^{-4}	7.45×10^{-4}	2.38×10^{-3}	3.68×10^{-3}	6.88×10^{-2}	1.05×10^{-1}
CO − 154(CO)	2.27×10^{-3}	1.35×10^{-3}	1.01×10^{-2}	2.70×10^{-2}	2.52×10^{-2}	3.58×10^{-1}	9.95×10^{-1}
CO − 154(CO)(Err)	2.53×10^{-4}	1.83×10^{-4}	6.41×10^{-4}	1.95×10^{-3}	2.82×10^{-3}	5.77×10^{-2}	1.00×10^{-1}
CO − 216(CO)	9.68×10^{-4}	5.53×10^{-4}	4.16×10^{-3}	1.22×10^{-2}	1.10×10^{-2}	1.60×10^{-1}	5.15×10^{-1}
CO − 216(CO)(Err)	9.70×10^{-5}	6.63×10^{-5}	2.73×10^{-4}	8.81×10^{-4}	1.36×10^{-3}	2.54×10^{-2}	3.81×10^{-2}
H I − region (Res)	2.78×10^{-2}	1.19×10^{-2}	-5.84×10^{-2}	-1.14×10^{-2}	-2.11×10^{-2}	1.40	-1.19×10^{-2}
H I − region (Res)(Err)	8.78×10^{-5}	6.75×10^{-5}	4.99×10^{-4}	8.81×10^{-4}	6.55×10^{-4}	1.57×10^{-2}	3.91×10^{-2}
CO − 154(Res)	6.60×10^{-2}	3.34×10^{-2}	-2.09×10^{-1}	-1.80×10^{-1}	-9.90×10^{-2}	2.92×10^{-1}	−4.31
CO − 154(Res)(Err)	2.65×10^{-4}	1.92×10^{-4}	6.71×10^{-4}	2.03×10^{-3}	2.94×10^{-3}	5.96×10^{-2}	1.02×10^{-1}
CO − 216(Res)	6.39×10^{-2}	3.38×10^{-2}	-5.64×10^{-1}	-5.22×10^{-1}	4.85×10^{-2}	−2.25	$-1.87 \times 10^{+1}$
CO − 216(Res)(Err)	2.65×10^{-4}	1.81×10^{-4}	7.45×10^{-4}	2.38×10^{-3}	3.68×10^{-3}	6.88×10^{-2}	1.05×10^{-1}

Notes. All values are normalized to $N_{\rm H} = 10^{20}$ H cm^{-2}. IRAC values are corrected for extended emission correction factors. Errors are $1 - \sigma$.

Table 6
DIRBE SED of the Various Components Studied Here

Name	DIRBE3	DIRBE4	DIRBE5	DIRBE6	DIRBE7	DIRBE8	DIRBE9	DIRBE10
MW (Plane)	4.30×10^{-3}	3.44×10^{-3}	5.09×10^{-2}	6.18×10^{-2}	4.84×10^{-1}	1.53	3.07	2.12
MW (Plane)(Err)	4.09×10^{-3}	3.44×10^{-3}	5.30×10^{-3}	9.33×10^{-3}	2.47×10^{-2}	4.59×10^{-2}	9.51×10^{-2}	6.58×10^{-2}
MW (Diff)	1.11×10^{-3}	1.76×10^{-3}	2.79×10^{-2}	2.90×10^{-2}	1.03×10^{-1}	6.04×10^{-1}	1.02	7.83×10^{-1}
MW (Diff)(Err)	2.39×10^{-5}	4.65×10^{-5}	5.10×10^{-4}	5.88×10^{-4}	1.85×10^{-3}	9.74×10^{-3}	2.14×10^{-2}	1.57×10^{-2}

Table 7
IRIS SED of the Various Components Studied Here

Name	*IRAS*1	*IRAS*2	*IRAS*3	*IRAS*4
MW (Plane)	5.68×10^{-2}	7.61×10^{-2}	5.21×10^{-1}	1.61
MW (Plane)(Err)	2.90×10^{-3}	1.15×10^{-2}	5.42×10^{-2}	2.17×10^{-1}
MW (Diff)	...	...	...	...
MW (Diff) (Err)	...	...	...	...
LMC_All	8.24×10^{-3}	2.15×10^{-2}	3.74×10^{-1}	7.75×10^{-1}
LMC_All(Err)	3.36×10^{-3}	4.51×10^{-3}	4.28×10^{-2}	1.24×10^{-1}
H I − region (H I)	1.39×10^{-2}	1.68×10^{-2}	2.09×10^{-1}	6.09×10^{-1}
H I − region (H I)(Err)	8.74×10^{-4}	1.29×10^{-3}	1.23×10^{-2}	2.61×10^{-2}
CO − 154 (H I)	3.45×10^{-2}	5.57×10^{-2}	7.33×10^{-1}	1.46
CO − 154 (H I)(Err)	1.97×10^{-3}	5.61×10^{-3}	4.93×10^{-2}	8.23×10^{-2}
CO − 216 (H I)	3.46×10^{-2}	3.10×10^{-2}	5.47×10^{-1}	1.23
CO − 216 (H I)(Err)	2.03×10^{-3}	4.99×10^{-3}	5.24×10^{-2}	8.80×10^{-2}
CO − 154(CO)	2.51×10^{-2}	4.25×10^{-2}	2.25×10^{-1}	5.13×10^{-1}
CO − 154(CO)(Err)	1.90×10^{-3}	5.39×10^{-3}	4.78×10^{-2}	8.04×10^{-2}
CO − 216(CO)	1.15×10^{-2}	1.72×10^{-2}	1.22×10^{-1}	2.90×10^{-1}
CO − 216(CO)(Err)	7.50×10^{-4}	1.84×10^{-3}	1.94×10^{-2}	3.20×10^{-2}
H I − region (Res)	-3.27×10^{-2}	-1.09×10^{-1}	2.69×10^{-1}	1.37
H I − region (Res)(Err)	8.74×10^{-4}	1.29×10^{-3}	1.23×10^{-2}	2.61×10^{-2}
CO − 154 (Res)	-3.93×10^{-1}	-7.24×10^{-1}	−2.66	−3.01
CO − 154 (Res)(Err)	1.97×10^{-3}	5.61×10^{-3}	4.93×10^{-2}	8.23×10^{-2}
CO − 216 (Res)	-6.58×10^{-1}	-1.64×10^{-2}	−5.89	$-1.15 \times 10^{+1}$
CO − 216 (Res)(Err)	2.03×10^{-3}	4.99×10^{-3}	5.24×10^{-2}	8.80×10^{-2}

REFERENCES

Abergel, A., et al. 1994, ApJ, 423, 59
Aguirre, et al. 2003, ApJ 596
Arendt, R. G., et al. 1998, ApJ, 508, 74
Asplund, M., Grevesse, N., & Sauval, A. J. 2004, A&A, 417, 751
Bernard, J. Ph., Boulanger, F., & Puget, J. L. 1993, A&A, 277, 609
Bernard, J. Ph., et al. 1994, A&A, 291, L5
Bernard, J. Ph., et al. 1999, A&A, 347, 640
Bica, E., Claria, J. J., Dottori, H., Santos, J. F. C., Jr., & Piatti, A. E. 1996, ApJS, 102, 57
Bloemen, J. B. G, et al. 1986, A&A, 154, 25
Bohlin, R. C., Savage, B. D., & Drake, F. J. 1978, ApJ, 224, 132
Bolatto, A. D., et al. 2007, ApJ, 655, 212
Bot, C., et al. 2004, A&A, 423, 567
Boulanger, F., et al. 1996, A&A, 312, 256
Clayton, G. C., & Martin, P. G. 1985, ApJ, 288, 558
Clayton, G. C., Martin, P. G., & Thompson, I. 1983, ApJ, 265, 194
Cohen, R. S., et al. 1988, ApJ, 331, L95
Davies, R. D., Elliott, K. H., & Meaburn, J. 1976, MNRAS, 81, 89
DeGioia-Eastwood, K. 1992, ApJ, 397, 542
Désert, F.-X., Boulanger, F., & Puget, J. L. 1990, A&A, 237, 215
Dickey, J. M., & Lockman, F. J. 1990, ARA&A, 28, 215
Dickey, J. M., Mebold, U., Stanimirovic, S., & Staveley-Smith, L. 2000, ApJ, 536, 756
Dickinson, C., Davies, R. D., & Davis, R. J. 2003, MNRAS, 341, 369
Diplas, A., & Savage, B. D. 1994, ApJ, 427, 274
Dufour, R. J. 1984, in Structure and Evolution of the Magellanic Clouds, ed. S. Van den Bergh, & K. S. de Boer (Dordrecht: Reidel), 596
Dwek, E., et al. 1997, ApJ, 475, 565
Engelbracht, C. W., et al. 2007, PASP, 119, 994
Fazio, G. G., et al. 2004, ApJS, 154, 10
Feast, M. 1999, in IAU Symp. 190, New Views of the Magellanic Clouds, ed. Y.-H. Chu, et al. (San Fransisco: ASP), 542
Flagey, N., et al. 2006, A&A, 453, 969
Fukui, Y., et al. 1999, PASJ, 51, 745
Fukui, Y., et al. 2008, ApJS, in press
Galliano, F., et al. 2003, A&A, 407, 159
Galliano, F., et al. 2005, A&A, 434, 867
Gaustad, J. E, McCullough, P. R., Rosing, W., & van Buren, D. 2001, PASP, 113, 1326
Gordon, K. D., et al. 2003, ApJ, 594, 279
Grenier, I., Casandjian, J. M., & Terrier, R. 2005, Science, 307, 1292
Hartmann, D., & Burton, W. B. 1995, Atlas of Galactic HI Emission (Cambridge, MA: Cambridge Univ. Press)
Israel, F. P., A&A, 328, 471
Jones, A. P., Tielens, A. G. G. M., & Hollenbach, D. J. 1996, ApJ, 469, 740
Kaufman, M., Wolfire, M. G., Hollenbach, D. J., & Luhman, M. L. 1999, ApJ, 527, 795
Keller, et al. 2006, ApJ, 642, 834
Kim, S., Dopita, M. A., Staveley-Smith, L., & Bessell, M. S. 1999, ApJ, 118, 2797
Kim, S., et al. 2003, ApJS, 148, 473
Kornreef, J. 1982, A&A, 107, 247
Lagache, G., Haffner, L. M., Reynolds, R. J., & Tufte, S. L. 2000, A&A, 354, 247
Laureijs, R. J., Clark, F. O., & Prusti, T. 1991, ApJ, 372, 185
Li, A., & Draine, B. T. 2002, ApJ, 576, 762
Leroy, A., et al. 2007, ApJ, 658, 1027
Lu, N. 2004, ApJ, 154, 286
Lu, N., et al. 2003, ApJ, 588, 199
Madden, S. C., Galliano, F., Jones, A. P., & Sauvage, M. 2006, A&A, 446, 877
Madden, S. C., et al. 1997, ApJ, 483, 200
Marx-Zimmer, M., et al. 2000, A&A, 354, 787
Massa, D., & Savage, B. D. 1984, ApJ, 279, 310
Meixner, M., et al. 2006, AJ, 132, 2268
Meyerdierks, H., & Heithausen, A. 1996, A&A, 313, 929
Misselt, K. A., Clayton, G. C., & Gordon, K. D. 1999, ApJ, 515, 128

Miville-Deschênes, M.-A., & Lagache, G. 2005, ApJSS, 157, 302
Mizuno, N., et al. 2001, PASJ, 53, 971
Mochizuki, K., et al. 1994, ApJ, 430, 37
Onishi, T., et al. 2001, PASJ, 53, 1017
Paladini, R., et al. 2007, A&A, 465, 839
Peeters, E., et al. 2002, A&A, 381, 571
Pei, Y. C., Fall, S. M., & Hauser, M. G. 1999, ApJ, 522, 604
Poglitsch, A., et al. 1995, ApJ, 454, 293
Reach, W. T., Wall, W. F., & Odegard, N. 1998, ApJ, 507, 507
Reach, W. T., et al. 2005, PASP, 117, 978
Reynolds, R. J. 2004, Adv. Space Res., 34, 27–34
Rieke, G. H., et al. 2004, ApJS, 154, 25
Russell, S. C., & Dopita, M. A. 1992, ApJ, 384, 508
Ryter, C., Puget, J. L., & Perault, M. 1987, A&A, 186, 312
Sakon, I., et al. 2006, ApJ, 651, 174
Sauvage, M., Vigroux, L., & Thuan, T. X. 1990, A&A, 237, 296
Schwering, P. B. W. 1989, A&A Suppl., 79, 105
Sellgren, K., Werner, M. W., & Dinerstein, H. L. 1983, ApJ, 271, L13
Solomon, P. M., et al. 1987, ApJ, 319, 730
Stanimirovic, S., et al. 2000, MNRAS, 315, 791
Staveley-Smith, L., et al. 2003, MNRAS, 339, 87
Stepnik, B., et al. 2003, A&A, 398, 511
Van der Marel, R., & Cioni, M. R.-L. 2001, AJ, 122, 1807
Vermeij, R., Peeters, E., Tielens, A. G. G. M., & Van der Hulst, J. M. 2002, A&A, 382, 1042
Werner, M. W., et al. 2004, ApJS, 154, 1
Westerlund, B. E. 1997, The Magellanic Clouds (New York: Cambridge Univ. Press)